Transdimensional Electrical Resistivity Tomography

Transdimensional Electrical Resistivity Tomography

E. Galetti[1], **A. Curtis**[1]

[1]University of Edinburgh, School of GeoSciences, James Hutton Road, Edinburgh EH9 3FE, United Kingdom

Key Points:

- Voronoi cells provide a more flexible inversion parameterisation compared to previous research
- Including full non-linearity allows us to image deeper into the solid Earth with the same data
- Uncertainty loop topologies are observed in multiple types of physics

Corresponding author: Erica Galetti, erica.galetti@ed.ac.uk

Abstract

This paper shows that imaging the interior of solid bodies with fully non-linear physics can be highly beneficial compared to imaging with the equivalent linearised tomographic methods, and that this is true for a variety of different types of physics. Including full non-linearity provides interpretable uncertainties, and far greater depth of image penetration into unknown targets such as the Earth's subsurface. We use an adaptively parameterised Monte Carlo method to invert electrical resistivity data for the conductivity structure of the Earth, and demonstrate the method on two field datasets. Key results include the observation of directly interpretable uncertainty loops which define possible geometrical variations in the edges of isolated anomalies, hence quantifying the spatial resolution of these boundaries. These topologies of uncertainties are similar to those observed when performing fully non-linear seismic travel time tomography. This shows that loop-like uncertainty topologies are expected in the solutions to a wide variety of tomographic problems, using a variety of data types and hence laws of physics (here the Laplace equation; in previous work the Eikonal or ray equations). We also show that the depth to which we can construct a tomographic image using electrical data is extended by up to a factor of 8 using non-linear methods compared to linearised inversion using common standard linearised programs. These advantages come at the cost of significantly increased computation. All of these results are illustrated on both synthetic and real data examples.

1 Introduction

Geophysical imaging methods are routinely employed in both industry and academia to obtain information about the composition of the Earth's subsurface and its changes over time. While in some cases one might be satisfied by finding the single model which best explains the recorded data, it may often be the case that a single best-fitting model is of little value to decision makers since a comprehensive assessment of risk may only be carried out by assessing the full range of possible models that fit our observations (i.e., the post-experiment or *posterior* distribution of models given the available data). This set of models and statistics of their distribution are commonly referred to as the model *uncertainty*. For instance, when geophysical methods are employed to evaluate the size of a subsurface plume of leaked fluids or to monitor its changes over time, an accurate evaluation of model uncertainty, the range of subsurface models that may be permissible, is necessary in order to assess the risk related to the volumes and rates of escaping fluids.

In a typical imaging scenario, geophysical data are acquired at the Earth's surface or within boreholes. Depending on the type of data acquired, inversion might be required in order to recover the subsurface properties of interest from the recorded quantities. Mathematically speaking, this involves inferring a set of model parameters $\mathbf{m}$ from a set of observed data $\mathbf{d}^{obs}$, and is achieved by solving an expression such as $\mathbf{d}^{obs} = \mathbf{d}^{true} + \epsilon = \mathbf{g}(\mathbf{m}) + \epsilon$ for $\mathbf{m}$, where $\mathbf{d}^{true}$ represents the data that would be recorded in the absence of sources of error, ϵ is an error term, and $\mathbf{g}$ is a function that describes the physics relating $\mathbf{m}$ to $\mathbf{d}^{true}$. In this framework, ϵ represents the effects on recorded data of any elements of the physics relating $\mathbf{d}^{obs}$ to $\mathbf{m}$ that are not represented within function $\mathbf{g}$. The distribution of possible values of ϵ therefore represents the uncertainties in the observed data when compared to $\mathbf{d}^{true} = \mathbf{g}(\mathbf{m})$. However note that in practical applications, $\mathbf{g}(\mathbf{m})$ is normally evaluated using numerical methods which involve a number of approximations in function $\mathbf{g}$, and which result in further sources of error.

In electrical resistivity tomography (ERT), electrical currents are actively injected into the ground from pairs of electrodes, and the resulting electrical potential is measured as the potential difference between other pairs of electrodes located on or below the Earth's surface. These measurements constitute a set of observations $\mathbf{d}^{obs}$, and are used to estimate the resistivity structure of the subsurface parameterised by vector $\mathbf{m}$. In ERT, the *forward problem* consists of finding a set of potential differences $\mathbf{d}^{pred}$ through resistivity model $\mathbf{m}$, which

can be calculated computationally by simulating the potential field induced within model $\mathbf{m}$ by the electric currents [*Dey and Morrison*, 1979a,b; *Pridmore et al.*, 1981]. The *inverse problem* involves inferring the set of models $\mathbf{m}$ such that $\mathbf{g}(\mathbf{m})$ matches the observed potential differences $\mathbf{d}^{obs}$ to within their observational uncertainties (since all such models in that set represent possible subsurface structures).

However, solving an inverse problem in geophysics poses challenges which go beyond merely finding a solution that mathematically fits observed data. It is almost always the case that more than one model $\mathbf{m}$ may adequately fit the observations $\mathbf{d}^{obs}$ to within their uncertainties. Inverse problems may be solved by using optimisation or stochastic (often Bayesian) methods. In an optimisation framework (e.g., *Parker* [1994]), the combination of parameters that minimises an objective function (involving data misfit and regularisation terms) is generally regarded as the model solution. This makes sense in cases where it does not particularly matter which solution is found out of the set of possible solutions (for example, when optimising the model parameterisation to best represent measured information [*Curtis and Snieder*, 2002], designing an optimal experiment or survey to constrain parameters [*Curtis*, 1999a,b; *Maurer et al.*, 2000], finding parameters that smoothly interpolate through data [*Sambridge et al.*, 1995], or where the problem is so large that it is computationally intractable to find more than one solution from the set [*Simmons et al.*, 2012]). By contrast, stochastic inversion schemes do not limit the solution to a single model but produce a large ensemble of valid models. Typically such methods are associated with Bayesian inversion where the desired set of models are distributed according to a so-called *posterior* probability density function (PDF), so that each model parameter has a distribution of possible values rather than a single value [*Mosegaard and Tarantola*, 1995; *Tarantola*, 2005]. Obviously, regardless of the inversion scheme employed, the solution to a geophysical inverse problem must also make sense physically.

Within the context of ERT, a number of authors have employed stochastic methods in order to overcome the problem of non-uniqueness and include prior information in the solution (e.g., *Kaipio et al.* [2000], *Ramirez et al.* [2005]). In addition, a number of studies have employed stochastic methods to invert direct current (DC) resistivity datasets jointly with other types of data. For instance, *JafarGandomi and Binley* [2013] use multiple types of geophysical datasets in a joint transdimensional McMC inversion algorithm combining data from DC resistivity, electromagnetic induction and ground penetrating radar (GPR); *Linde et al.* [2006] invert DC resistivity and GPR traveltime data with a regularised least-squares algorithm, but use stochastic regularization operators based on geostatistical models to constrain the solution; *Irving and Singha* [2010] use McMC to jointly invert DC resistivity and borehole tracer concentration data to obtain posterior information on hydraulic conductivity; *Jardani et al.* [2013] perform a fully-coupled inversion of hydrogeochemical and geolectrical data by combining DC resistivity, self-potential, and salinity measurements.

Data uncertainties play a fundamental role in geophysical inverse problems as they determine how accurately the model should fit observed data. Sources of uncertainty in geophysical inversion are diverse and normally include contributions from both data measurement and modelling errors. In the context of ERT, measurement errors might for instance be caused by inaccuracy of the voltmeter and/or ammeter and electrode charge-up effects, while modelling errors are typically due to approximations in the physics of the forward problem represented by function $\mathbf{g}$ or in the numerical methods used to evaluate $\mathbf{g}(\mathbf{m})$ for any $\mathbf{m}$, and to the mislocation of electrodes in the acquisition array leading to geometrical errors. Given the presence of contaminating noise during acquisition and the limitations in instrumental sensitivity, resolution, and computational power, such errors are unavoidable and must be accounted for correctly when evaluating the uncertainty associated with the set of solutions to the inverse problem. For instance, in cases where ERT is used to evaluate the size of a leakage plume or to monitor its changes over time, the solution must include an estimate of uncertainty in order to correctly assess the spatial resolution of the plume through inversion or whether leakage is still ongoing. Hence, in situations where assessing the veracity of a

particular potential event or hypothesis is paramount, the use of stochastic, rather than optimisation, inversion methods is particularly beneficial since an estimate of model uncertainty can be evaluated directly from the posterior PDF of each model parameter.

However, the benefits of stochastic tomography methods are often accompanied by increases in the computational time and resources required to perform the inversion. In the case of ERT, such increases are mainly due to the repeated computation of the forward problem which must be solved tens or hundreds of thousands of times. A number of authors have attempted to mitigate the computational expense of stochastic ERT by reducing the size of the space of plausible solutions. For instance, *Ramirez et al.* [2005] use prior information to parameterise subsurface contaminant plumes as a set of simple volumes embedded in a homogeneous medium, and combine Markov chain Monte Carlo (McMC) with 3D ERT to monitor changes in the shape and size of the plumes with time; *Rosas-Carbajal et al.* [2014] employ a smoothing constraint in joint ERT and RMT inversion to favour models showing smooth spatial transitions, hence decreasing the size of the model space to those satisfying this constraint; and *Andersen et al.* [2003] define the model in terms of a set of vertices which can be joined to create polygons whose number and size is determined by a set of user-defined tuning parameters.

Within this paper we present a stochastic inversion method for resistivity tomography which uses Bayesian theory [*Bayes and Price*, 1763], the reversible-jump Markov chain Monte Carlo algorithm (rj-McMC – *Green* [1995, 2003]), and model parameterisation with Voronoi cells [*Bodin et al.*, 2009; *Bodin and Sambridge*, 2009] to solve the inverse problem of ERT and to produce an ensemble of valid solutions which are distributed according to the Bayesian posterior PDF. This method can be referred to as 'transdimensional' in that the dimensionality of the model space (the number of model parameters) is allowed to vary between different models. Transdimensional inversion is a relatively new concept in electrical resistivity tomography, but has previously shown great potential in tackling a number of diverse inverse problems such as regression [*Gallagher et al.*, 2011], inversion of frequency-domain [*Minsley*, 2011] and controlled source [*Ray et al.*, 2014] electromagnetic data, geoacoustic inversion of seabed reflection coefficients [*Dettmer et al.*, 2010], inversion of surface-wave phase and group velocities [*Young et al.*, 2013] and traveltimes [*Bodin and Sambridge*, 2009; *Galetti et al.*, 2015], joint inversion of surface-wave dispersion and receiver function data [*Bodin et al.*, 2012a], inversion of DC resistivity sounding curves [*Malinverno*, 2002], and full waveform inversion of marine seismic data [*Ray et al.*, 2016]. In addition, *Hawkins and Sambridge* [2015] recently developed a new class of transdimensional solvers that sample over tree structures, and this sampling approach has successfully been applied in 2D to the time-domain electromagnetic inverse problem [*Hawkins et al.*, 2017] and to seismic low-frequency full waveform inversion *Ray et al.* [2018].

One advantage of a transdimensional approach lies in the fact that, by allowing the model parameters (in our case the number of Voronoi cells used to discretise the Earth's subsurface resistivity structure) to vary in number, shape and size, the space of possible a priori parameterisations is broadened, ensuring a more comprehensive estimation of the a posteriori uncertainty since this becomes independent of any particular choice of model parameterisation. In addition, thanks to the 'natural parsimony' of Bayesian inference, posterior models are only as complex as is required by the data or by prior information: among similar models that provide equal fit to the observations, simpler ones (those having fewer Voronoi cells) are assigned a higher probability since larger prior volumes are penalised. A mathematical proof of this concept is given by *Ray et al.* [2016, 2018], who describe 'natural parsimony' as the result of a trade-off between Occam Factor (i.e., the ratio of posterior accessible volume to prior accessible volume [*MacKay*, 2003]) and high likelihood (low misfit), and how this trade-off automatically provides a solution similar to regularisation but largely dependent on the data. Finally, by reducing the model space dimensionality to only what is required to explain the data, one avoids over-parameterising the space of solutions. The computational demands of stochastically exploring higher-dimensional spaces explodes exponentially

(called the *curse of dimensionality – Scales and Snieder* [1997], *Curtis and Lomax* [2001]), so the natural parsimony also enormously reduces the computation required to find the solution set by limiting its number of dimensions. In turn, this makes uncertainty estimation tractable.

In the next section, we provide an overview of the forward problem in electrical resistivity tomography and present the transdimensional electrical resistivity tomography (TERT) method, showing how it can be used to perform a fully non-linear inversion of potential difference measurements. In Section 3, we present results of two synthetic experiments in which TERT was used to perform the inversion, and compare the results to those obtained using a more traditional, iterative-linearised inversion method. In Section 4, we apply TERT to a real dataset acquired at an archaeological site in Scotland, and we present a further observational example using a dataset acquired at an archaeological site in Slovakia in the online Supporting Information. We then discuss the main advantages and disadvantages of this method, and outline directions for future work before concluding.

2 Method

2.1 The forward problem

In electrical resistivity imaging, pairs of 'current electrodes', located either on the Earth's surface or within boreholes, are used to inject electrical currents into the ground, while the resulting electric potentials are measured by pairs of many 'potential electrodes' along an array. The forward problem therefore consists of solving the following equation for the electrical potential $\Phi(\mathbf{x})$ at each potential electrode location, and calculating potential differences between many pairs of electrodes:

$$\nabla \cdot \left[\frac{1}{\rho(\mathbf{x})} \nabla \Phi(\mathbf{x}) \right] = -I \left(\delta(\mathbf{x} - \mathbf{x}_+) - \delta(\mathbf{x} - \mathbf{x}_-) \right) \tag{1}$$

where $\rho(\mathbf{x})$ denotes resistivity at location $\mathbf{x}$, and $\mathbf{x}_+$ and $\mathbf{x}_-$ represent the location of a positive and negative current electrode, respectively (for completeness, the simpler case of current injection from a single electrode is described in Appendix A:).

Analytical solutions to equation 1 can be found for simple cases such as a buried sphere in a homogeneous medium or a vertical boundary separating two media of different resistivity (see examples in *Telford et al.* [1991]). However, more sophisticated numerical techniques are needed when the resistivity structure of the subsurface is more complex. Such techniques include the linear filter method in 1D (e.g., *Koefoed* [1979]), and finite-difference and finite-element methods in 2D and 3D (e.g., *Dey and Morrison* [1979a,b]; *Pridmore et al.* [1981]).

Many authors have developed linearised numerical techniques and programs to solve equation 1 for complex resistivity geometries $\rho(\mathbf{x})$ in 2D and 3D [*Dey and Morrison*, 1979a,b; *Pridmore et al.*, 1981; *Lowry et al.*, 1989; *Loke*, 1994; *Li and Spitzer*, 2002; *Rücker et al.*, 2006; *Pidlisecky and Knight*, 2008; *Binley*, 2013a,b]. Within our inversion algorithm, we solve the forward problem using a finite-difference scheme adapted from the MATLAB modelling code *FW2_5D* by *Pidlisecky and Knight* [2008]. Besides being completely open source and easily understood, *FW2_5D* is a highly efficient and customizable code, and we easily optimised and integrated it into our own inversion program. The forward modelling routines in *FW2_5D* are based on the 2.5D modelling algorithm of *Dey and Morrison* [1979a] in which subsurface structures are described in 2D (i.e., they are assumed to be constant along the y direction) but the current flow is modelled in all three dimensions using a Fourier-cosine transform. Hence, the 3D physics of current flow is accounted for without the need for far more expensive three dimensional modelling. Nevertheless, since the inversion algorithm is entirely separate from the forward calculations, the forward modeller could easily be replaced by alternative routines.

2.2 Inversion with the rj-McMC algorithm

The rj-McMC algorithm by *Green* [1995] was first applied to geophysical tomography problems by *Bodin and Sambridge* [2009], who implemented this method within a linearised, iterative seismic traveltime inversion scheme. In each iteration they used the rj-McMC algorithm to produce an ensemble of velocity models which fit the observed traveltime data, but with fixed ray paths (thus linearising the problem). The forward problem of calculating source-receiver traveltimes was then solved using the average velocity structure obtained from the ensemble of models to fix seismic ray paths for the next iteration. In doing so, *Bodin and Sambridge* [2009] partly accounted for the non-linearity of the tomographic problem since raypaths and traveltimes were updated at the end of each Markov chain loop. Later, *Galetti et al.* [2015] modified their algorithm to make it fully nonlinear: in the approach of *Galetti et al.* [2015], the forward problem was solved for every individual model in the ensemble, thus no linearisation-related forward modelling approximations and biases were introduced into the solution.

Within this study, we adapted the approach of *Galetti et al.* [2015] to the inverse problem of ERT in order to produce a fully nonlinear inversion method. Similarly to *Bodin and Sambridge* [2009] and *Galetti et al.* [2015], this method uses an irregular Voronoi cell tessellation to parameterise the model and allows uncertainty in the solution to be estimated correctly. In this section, we review the rj-McMC tomography framework of *Bodin and Sambridge* [2009] by providing an overview of the model parameterisation employed and describing the Bayesian approach used by the algorithm. Further details on the mathematical theory behind the algorithm can be found in Appendix B: .

2.2.1 Bayes' theorem

Within a Bayesian framework, information is represented by probability density functions. Bayesian inference makes use of Bayes' theorem [*Bayes and Price*, 1763] to estimate the *a posteriori* PDF (also known as 'posterior distribution') $p(\mathbf{m}|\mathbf{d}^{obs})$, which can be defined as the probability density of model $\mathbf{m}$ given observed data $\mathbf{d}^{obs}$. Bayes' theorem states that $p(\mathbf{m}|\mathbf{d}^{obs})$ can be estimated by combining information from observations with *a priori* information about the model according to

$$p(\mathbf{m}|\mathbf{d}^{obs}) \propto p(\mathbf{d}^{obs}|\mathbf{m})p(\mathbf{m}) \tag{2}$$

Here, $p(\mathbf{d}^{obs}|\mathbf{m})$ is called the likelihood function, which expresses the probability of observing dataset $\mathbf{d}^{obs}$ given model $\mathbf{m}$, and prior information about model $\mathbf{m}$ (i.e., everything we knew about the model before performing the inversion) is represented by the *prior* probability density $p(\mathbf{m})$. Equation 2 therefore represents how prior information about the model is updated by new data to give the posterior state of information described by $p(\mathbf{m}|\mathbf{d}^{obs})$.

2.2.2 Model parameterisation with Voronoi cells

Our implementation of the rj-McMC algorithm in ERT uses Voronoi cells to parameterise the resistivity model. A Voronoi tessellation of a 2D xz plane of resistivity values is achieved by defining a set of n nuclei (the black dots in Figure 1) which are identified by their xz coordinates, and a value of $\log_{10}$(resistivity) for each nucleus. For simplicity, from here onwards we drop the subscript in $\log_{10}$ and simply denote the logarithm in base 10 as log. The 2D plane is then divided into n non-overlapping regions (Voronoi cells) of different resistivity such that each region contains the portion of the plane which is closest to its nucleus. Note that Voronoi nuclei are not necessarily located at the centre of their corresponding cells, but rather cell boundaries are defined by the perpendicular bisectors of pairs of neighbouring nuclei. A resistivity model can therefore be defined as $\mathbf{m} = [n, \mathbf{c}, \boldsymbol{\mu}]$, where $\mathbf{c}$ and $\boldsymbol{\mu} = \log(\boldsymbol{\rho})$ are n-row arrays of nuclei xz coordinates and log(resistivity) values, respectively. In our implementation resistivity is constant within each Voronoi cell so the dimension of model $\mathbf{m}$ is $3n + 1$.

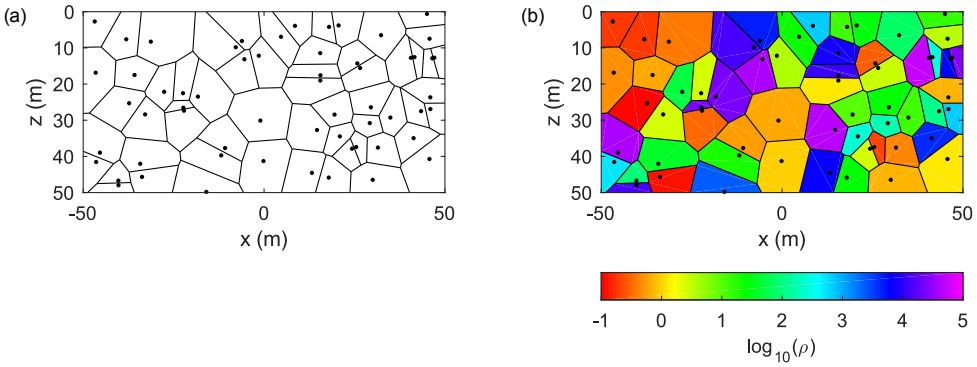

Figure 1. Example of Voronoi tessellation of a 2D plane. (a) Each Voronoi cell is identified by the location of its nucleus (black dots), and cell boundaries are defined purely by the perpendicular bisectors of pairs of neighbouring nuclei (black lines). (b) The Voronoi tessellation is turned into a resistivity model by assigning a value of log(resistivity) to each cell.

During the inversion, the location and number of Voronoi nuclei in the model is allowed to vary, making the number of Voronoi cells in the model one of the inversion parameters. Since Voronoi cells change shape and size throughout the inversion, the model parameterisation dynamically adapts to the spatial distribution of both information and subsurface structure.

2.2.3 Data noise parameterisation

Within a transdimensional inversion framework, the magnitude of data uncertainties influences the level of complexity (here, the number of Voronoi cells) in the final solution. In a similar framework for seismic traveltime tomography, *Bodin et al.* [2012b] proposed a method to parameterise uncertainty which allows data noise to be varied and estimated during the inversion. As the use of accurate uncertainties prevents data over- or under-fitting, so doing allows the observations to be fit up to the appropriate uncertainty level, and makes the rj-McMC method almost entirely data-driven.

If data uncertainty estimates are available, then those *a priori* uncertainties σ^{prior} (scaled arbitrarily in absolute terms) may be up- or down-scaled by a factor λ which can be estimated during inversion. Hence, for datum k with *a priori* uncertainty σ_k^{prior}, the *a posteriori* uncertainty σ_k^{post} is given by

$$\sigma_k^{post} = \lambda \times \sigma_k^{prior} \tag{3}$$

Since λ is an additional parameter to be determined during the inversion, this makes the dimension of the model equal to $3n + 2$. If multiple independent datasets with potentially different data noise levels are combined such that a λ value is determined for each dataset, the model dimension becomes $3n + n_{ds} + 1$, where n_{ds} is the number of datasets.

If no information on data uncertainties is available, data noise must be estimated during inversion since evaluating the data fit of any model requires that the uncertainty of each datum be taken into account. Although a single uncertainty value could be assigned to all measurements, in real acquisition scenarios it is likely that each measured potential difference will be affected by a different amount of noise. For instance, *Binley et al.* [1995] suggest a type of data noise parameterisation in which data variance (the square of data standard deviation) increases linearly with the square of the measured resistance R (the measured potential difference divided by the injected current) as in

$$(\sigma_k^{post})^2 = a^2 \times R^2 + b^2 \tag{4}$$

where a and b represent hyperparameters that could be estimated during the inversion. This type of data noise parameterisation makes the model dimension equal to $3n + 3$ if a single a and b are estimated for the entire dataset, and $3n + 2 \times n_{ds} + 1$ if n_{ds} datasets with different a and b parameters are combined.

When data noise is parameterised and estimated during the inversion, the model is defined by the combined set $\mathbf{m} = [n, \mathbf{c}, \boldsymbol{\mu}, \mathbf{h}]$, where $\mathbf{h}$ is the array of vector hyperparameters ($\mathbf{h} = [\lambda_1, \lambda_2, ...]$ or $\mathbf{h} = [a_1, b_1, a_2, b_2, ...]$), and where n, $\mathbf{c}$ and $\boldsymbol{\mu}$ are defined in Section 2.2.2.

However, note that data uncertainty estimation in ERT is an ongoing topic of research, hence a more sophisticated type of parameterisation for data uncertainties may be developed in future. For instance, *Tso et al.* [2017] recently highlighted how ERT measurement errors may not be uncorrelated as is often assumed, and developed an error model that includes the effect of the combination of electrodes used for each measurement as well as the linear relationship between measurement error and transfer resistance (equation 4). In addition, note that the term 'noise' in this paper refers to *both* measurement and modelling errors, hence the posterior uncertainty σ_k^{post} in equations 3–4 encapsulates any effect by which the model cannot explain the observed data.

2.2.4 A transdimensional Bayesian approach to tomography

As shown in equation 2, Bayesian inference is a valuable method to characterise the posterior PDF $p(\mathbf{m}|\mathbf{d}^{obs})$ by combining prior information with measured data. However, since the posterior PDF cannot normally be expressed in analytic form, it must be evaluated numerically at different positions in the model parameter space which involves solving the forward problem at each position. If the inverse problem has many dimensions as is usually the case in geophysics, the number of forward functions that need to be solved to explore the full parameter space becomes huge, making uniform sampling of the posterior computationally infeasible (e.g., *Curtis and Lomax* [2001]) and the use of alternative sampling methods a necessity.

Markov chain Monte Carlo (McMC) provides an iterative stochastic framework which generates samples from the Bayesian posterior PDF as expressed in equation 2. Using an McMC sampler such as the Metropolis-Hastings (MH) algorithm [*Metropolis et al.*, 1953; *Hastings*, 1970], samples are generated in sequence along a chain, each sample being a random perturbation of the one that precedes it. The initial model of the chain is selected randomly from the prior distribution described in the previous section, and often a randomly-selected model parameter or combination of parameters is perturbed at each step of the chain. However, compared to traditional McMC, the reversible jump Markov chain Monte Carlo (rj-McMC) algorithm [*Green*, 1995] does not fix the dimensionality of the model, hence 'jumps' in model dimensionality can also be made by adding or deleting model parameters (in our case Voronoi cells).

Our algorithm essentially consists of the following seven steps, which are displayed in the workflow diagram in Figure 2:

1. An initial resistivity model $\mathbf{m}$ is drawn from a Uniform distribution of Voronoi-tessellated models and data noise parameters.
2. Potential differences for all required configurations of current and potential electrodes are calculated through $\mathbf{m}$ (see Section 2.2.6 for implementation details in a Voronoi-cell model).
3. A new model $\mathbf{m}'$ is proposed by randomly perturbing the current model $\mathbf{m}$ using one of the following types of perturbation: *birth* to add a cell; *death* to delete a cell; *move* to change the location of a cell; *resistivity* to change the resistivity of a cell; *noise* to change a data noise parameter (see Appendix B.3 for more details on each perturbation type).

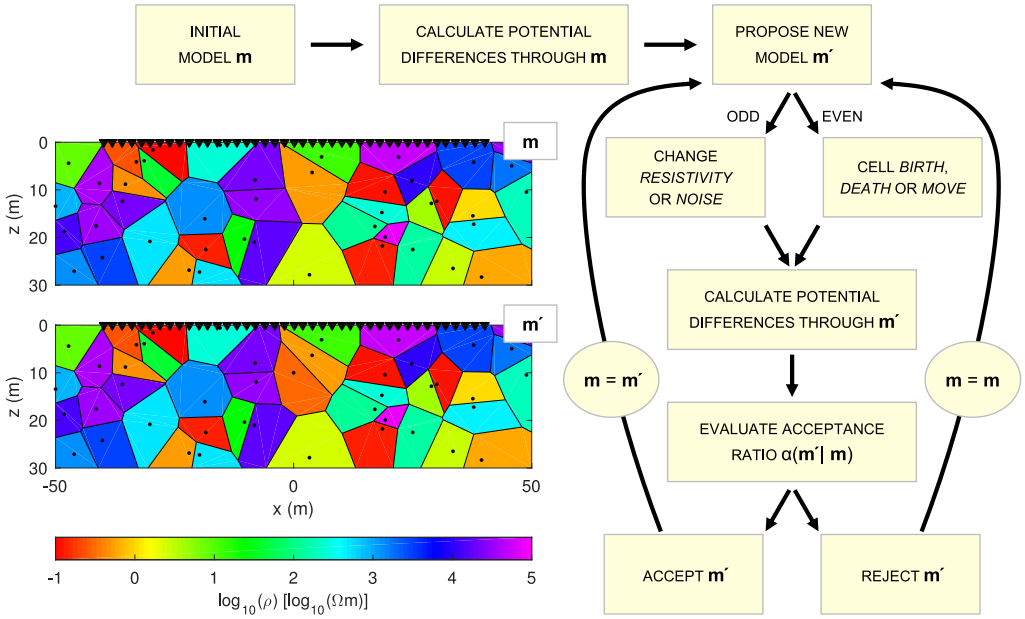

Figure 2. Workflow of the transdimensional electrical resistivity tomography (TERT) method. This samples the posterior PDF by producing an ensemble of Voronoi-tessellated models of subsurface resistivity using the rj-McMC algorithm. Each Voronoi cell is defined by the location of its nucleus (the black dots in $\mathbf{m}$ and $\mathbf{m}'$) and a value of log(resistivity) (log(ρ)). In this example, the geometry of model $\mathbf{m}$ is perturbed in a *birth* step by adding a Voronoi nucleus at [0 10] m.

4. Potential differences for all required configurations of current and potential electrodes are calculated through $\mathbf{m}'$ (note that no forward computations are needed for a *noise* step).
5. The acceptance ratio $\alpha(\mathbf{m}'|\mathbf{m})$ is calculated according to the following equation [*Bodin and Sambridge*, 2009]:

$$\alpha(\mathbf{m}'|\mathbf{m}) = \min\left[1, \frac{p(\mathbf{m}')}{p(\mathbf{m})} \times \frac{p(\mathbf{d}^{obs}|\mathbf{m}')}{p(\mathbf{d}^{obs}|\mathbf{m})} \times \frac{q(\mathbf{m}|\mathbf{m}')}{q(\mathbf{m}'|\mathbf{m})} \times |\mathbf{J}|\right] \quad (5)$$

   where the second term in the square bracket involves the product of the prior, likelihood and proposal ratios for $\mathbf{m}$ and $\mathbf{m}'$, and the Jacobian of the transformation from $\mathbf{m}$ to $\mathbf{m}'$ (see Appendix B.4 for a more detailed description of equation 5).
6. Depending on the value of $\alpha(\mathbf{m}'|\mathbf{m})$, the chain goes back to step 3 after either accepting or rejecting the proposed model $\mathbf{m}'$. If $\alpha \geq r$ where r is a random deviate from a Uniform distribution between 0 and 1, the change is accepted, and $\mathbf{m}'$ replaces $\mathbf{m}$ as the new current model. If $\alpha < r$, the change is rejected, $\mathbf{m}'$ is discarded, and model $\mathbf{m}$ is retained as the sample from this iteration.
7. Iterate from step 3 until sufficient samples have been generated.

Multiple chains are normally run independently of one another in parallel, ensuring that a larger volume of the model space is explored by starting the chains from different initial conditions. In addition, by solving the forward problem at each Markov chain iteration, we ensure that the non-linearity of the forward and inverse problems are fully accounted for and that no modelling-related approximations and biases are introduced into the solution.

At the end of the inversion, an ensemble of representative posterior samples is obtained by discarding the first few hundred thousand iterations from each Markov chain as 'burn-in' (samples that might still be biased by the initial randomly-chosen sample), and by retain-

ing only one model every few tens or hundreds of iterations thereafter to ensure that each sample in the ensemble is approximately independent of others (since consecutive samples in Markov chains can be strongly correlated). In practice, there are no hard and fast rules for choosing a burn-in period and a thinning interval, and some studies even suggest that thinning may not always be necessary [*Link and Eaton*, 2011]. However, a number of studies provide diagnostics that can be used to select and tune these parameters. For instance, Markov chain convergence may be assessed by comparing between-chain and within-chain variances for each model parameter [*Gelman and Rubin*, 1992; *Brooks and Gelman*, 1998], and the autocorrelation of posterior model parameters may be used to obtain an estimate of an appropriate thinning interval (e.g., *Aster et al.* [2013]). Within our study, we selected the burn-in period for each example by visually analysing plots displaying the change in misfit and number of cells with sample number across all Markov chains, discarding an initial window of samples for which these quantities had not yet stabilised. In terms of thinning, our choices were mainly dictated by a compromise between allowing enough separation between samples and having a large enough ensemble of samples within a reasonable computation time. Further details on Markov chain convergence are given in Section 5.2.

The posterior PDF on log(resistivity) at different locations in the subsurface can then be calculated from the ensemble by defining a regular grid of discrete points $[\bar{x}_i \;\; \bar{z}_i]$, extracting log(resistivity) at each grid point in each sample in the ensemble, and binning all of the posterior log(resistivity) values extracted at each point into a histogram. Maps showing different statistical properties of the subsurface resistivity field can also be obtained from the ensemble by calculating a number of statistical moments at each of these discrete points over the M samples in the ensemble, and merging these points together in order to create 2D maps of these statistical moments (see Appendix B.5 for details). However, it is important to emphasize that none of these statistics alone provides comprehensive information about the solution to the inverse problem; each should be considered within the context of a fully probabilistic solution.

Alternatively, the posterior probability distribution may be visualised in terms of marginal histograms of resistivity with depth (i.e., across all z locations for a particular horizontal position x) or with horizontal position (i.e., across all x locations for a particular depth z). While we do not present such plots herein, the reader is referred to *Bodin et al.* [2012a] and *Ray et al.* [2018] for examples of such plots in 1D and 2D, respectively.

2.2.5 Parallel tempering

As in any McMC scheme, convergence in rj-McMC inversion may be substantially hampered if Markov chains effectively become trapped while exploring local likelihood maxima. This normally occurs when the maximum being explored is surrounded by relatively low-likelihood models; the Markov chain tends to reject steps that would move from high to low likelihood due to the proposal ratio term in equation 5, so the chain only progresses from one maximum to another with very low probability, hence usually only after many attempts or steps.

This issue is normally overcome by running multiple independent Markov chains in parallel, ensuring that different parts of model space can be explored at the same time by following different random walks. In addition, the likelihood function may be 'tempered' by assigning a different temperature T_l to each of the L parallel chains [*Swendsen and Wang*, 1987; *Earl and Deem*, 2005; *Sambridge*, 2014]. By doing so, the likelihood becomes a function of model $\mathbf{m}_l$ and temperature T_l:

$$\mathcal{L}(\mathbf{m}_l, T_l) = p(\mathbf{d}^{obs}|\mathbf{m}_l)^{1/T_l} \tag{6}$$

where we drop the dependence of $\mathcal{L}$ on data $\mathbf{d}^{obs}$ for notational convenience since $\mathbf{d}^{obs}$ is measured and hence fixed. When $T_0 = 1$, the tempered likelihood $\mathcal{L}(\mathbf{m}_0, 1)$ is the same as that from equation 2, and the chain at $T_0 = 1$ is referred to as the *target* chain. When

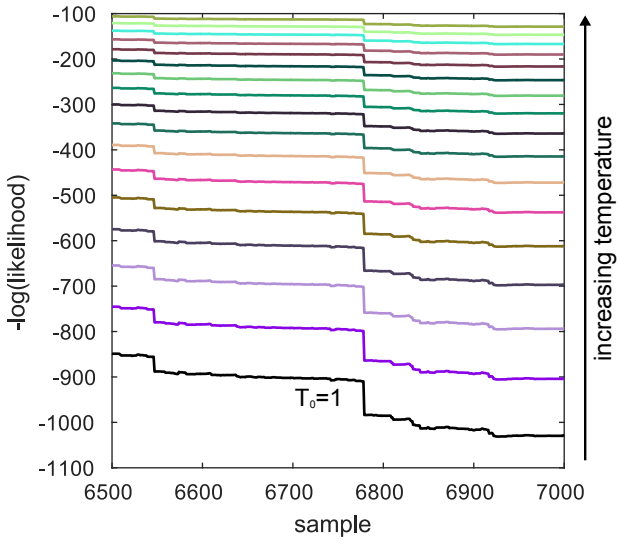

Figure 3. An example of tempered likelihood, calculated from equation 6 at increasingly higher temperatures (equally spaced on a logarithmic scale) from the target temperature $T_0 = 1$ (black line) to the highest temperature $T_l = 8$. The likelihood at the target temperature was calculated by running a Markov chain at $T_0 = 1$ using the synthetic dataset from Section 3.1. The other chains use the same samples but with recalculated tempered likelihoods according to equation 6.

$T_l > 1$, the likelihood function $\mathcal{L}(\mathbf{m}_l, T_l)$ is a smoother version of the untempered likelihood $p(\mathbf{d}^{obs}|\mathbf{m}_0)$ (i.e., it has lower 'relief' with flatter peaks and valleys), and it is therefore easier for a chain to explore since regions of high probability can be escaped more readily. As an example, Figure 3 shows the likelihood calculated along the same Markov chain run for the synthetic example described in Section 3.1 at the target temperature $T_0 = 1$ (black) and recalculated using equation 6, at 16 increasingly higher temperatures equally spaced in $\log(T)$, up to $T_l = 8$.

At each Markov chain iteration, any two randomly-chosen chains at different temperatures are allowed to exchange states (models) using the following Metropolis-Hastings acceptance criterion:

$$\alpha_{swap} = \min\left[1, \frac{\mathcal{L}(\mathbf{m}_{hot}, T_{cold})}{\mathcal{L}(\mathbf{m}_{hot}, T_{hot})} \times \frac{\mathcal{L}(\mathbf{m}_{cold}, T_{hot})}{\mathcal{L}(\mathbf{m}_{cold}, T_{cold})}\right] \tag{7}$$

where $T_{hot} > T_{cold}$, and $\mathbf{m}_{hot}$ and $\mathbf{m}_{cold}$ are the current models on the 'hot' and 'cold' chain, respectively. Hence, the expression $\mathcal{L}(\mathbf{m}_{hot}, T_{cold})$ corresponds to evaluating equation 6 using the model on the 'hot' chain $\mathbf{m}_{hot}$ and the 'cold' temperature T_{cold}. The swap is accepted if $\alpha_{swap} \geq r$, where r is a random deviate from a Uniform distribution between 0 and 1, and rejected otherwise. Note that, as suggested by *Sambridge* [2014], the exchange swaps are not restricted to neighbouring temperature levels, but are allowed between any pair of randomly-chosen levels.

Swapping models between chains at different temperatures promotes inter-chain mixing and allows local likelihood maxima to be escaped, ultimately speeding up convergence to the posterior PDF. This is particularly beneficial in cases where forward modelling calculations are computationally expensive so that considerable computing time may be spent on a single Markov chain iteration. Examples of applications of parallel tempering to geophysical inverse problems include the inversion of controlled-source electromagnetic data [*Ray et al.*, 2013], finite-fault [*Dettmer et al.*, 2014] and direct-seismogram [*Dettmer et al.*, 2015] inversion, the inversion of surface wave dispersion and receiver function data [*Roy and Romanowicz*, 2017], seismic body-wave [*Bottero et al.*, 2016] and ambient-noise [*Valentová*

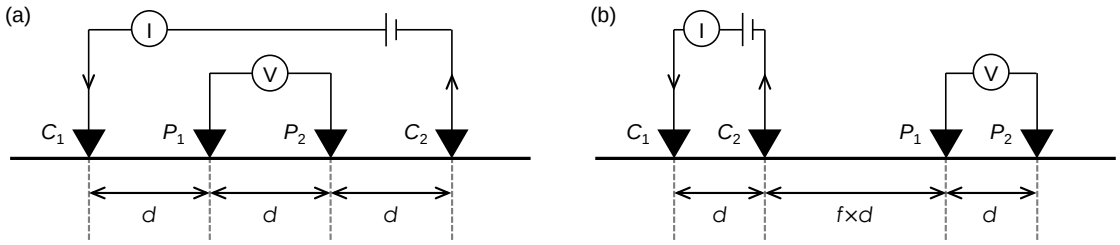

Figure 4. Electrode geometries used for the experiments described in this paper. Current electrodes are located at C_1 and C_2, and potential electrodes are located at P_1 and P_2. (a) In a Wenner-alpha array, electrodes are equally spaced with separation d. (b) In a dipole-dipole array, current and potential electrodes have the same spacing d, and the two dipoles C_1–C_2 and P_1–P_2 are separated by distance $f \times d$ (where f is generally an integer value).

et al., 2017] tomography, inversion of airborne electromagnetic data *Hawkins et al.* [2017], and full-waveform inversion of marine seismic data [*Ray et al.*, 2018].

In all of the examples presented in this paper, we performed TERT by running 32 Markov chains in parallel, and setting 16 chains at temperature $T_0 = 1$ (the *target* temperature) and 16 chains at log-uniformly spaced increasing temperatures up to $T_l = 8$ (the 'hottest' temperature). Posterior inferences were made only from samples in the chains at the *target* temperature (but these are influenced by the other chains through equation 7). Alternatively, samples at higher temperatures could be re-weighted to $T_0 = 1$ using an appropriate weighting function [*Brooks and Neil Frazer*, 2005; *Dosso et al.*, 2012], and added to the posterior ensemble.

2.2.6 Implementation details

Since the finite-difference forward modeller that we employed requires the resistivity structure to be defined on a regular grid of points, at each Markov chain iteration we sampled the Voronoi-tessellated resistivity model over a regular grid and solved the forward problem using this grid. In addition, given that resistivity values can span several orders of magnitude in Earth science scenarios, our inversion routine was set up to invert for $\mu = \log(\rho)$ rather than absolute resistivity values.

Finally, in its current implementation, our inversion code does not allow for topography to be taken into account. However, given that the forward modelling routine is completely separate from the inversion algorithm, the forward modeller could easily be swapped with one in which topography is considered, and where the z-coordinate of the Voronoi nuclei represents the depth of the nucleus below the Earth's surface.

3 Synthetic experiments

In order to test the effectiveness of the TERT method, we performed a number of synthetic tests using different resistivity models and acquisition geometries (Figure 4). We benchmarked our results against those obtained from a well known iterated-linearised inversion code (*R2* by *Binley* [2013b]). These experiments are presented below.

3.1 Example 1

In this first experiment we created a synthetic dataset for the simple resistivity model shown in Figure 5(a) using the forward modelling functions in *FW2_5D*. Using a Wenner-

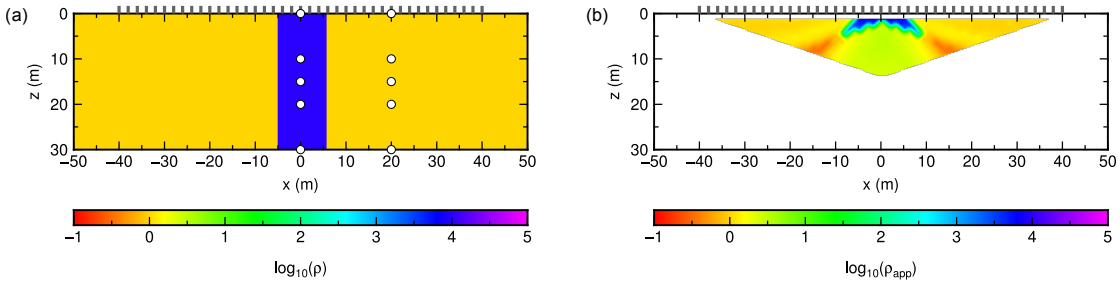

Figure 5. Synthetic resistivity model for the example application described in Section 3.1. (a) True resistivity section. (b) Resistivity pseudosection acquired using a Wenner-alpha configuration for 41 electrodes located between -40 and 40 m, with a minimum and a maximum spacing of $d = 2$ and $d = 26$ m in the geometry shown in Figure 4(a). A resistivity pseudosection is a contour plot where each datum (i.e., apparent resistivity calculated using equation 8 for a Wenner-alpha configuration) is plotted horizontally at the mid-point of the set of 4 electrodes used for the measurement, and vertically at the median depth of investigation [*Edwards*, 1977] of the electrode array used. In panel (a), the white circles denote the location of the points at which the posterior PDFs on log(resistivity) in Figure 6 were calculated. In both panels, the grey ticks at $z = 0$ m denote electrode locations.

alpha configuration (Figure 4(a)) with 41 electrodes located at regular intervals of 2 m, we modelled 260 potential differences for different combinations of current and potential electrodes with a minimum and maximum d spacing of 2 and 26 m, respectively. In order to emulate real scenarios where measurements are contaminated by noise, each computed potential difference k was perturbed by random Gaussian noise with standard deviation σ_k^{prior} equal to 3% of the measurement, which was then considered as the *prior* data noise level during inversion. The apparent resistivity pseudosection is shown in Figure 5(b). In order to generate this image, each modelled potential difference ΔV_k was first converted to apparent resistivity according to

$$\rho_{app_k} = 2\pi d \frac{\Delta V_k}{I_k} \tag{8}$$

where I_k denotes the injected current, and then plotted in a contour plot where each datum is located horizontally at the mid-point of the set of 4 electrodes used for the measurement, and vertically at the median depth of investigation [*Edwards*, 1977] of the electrode array used.

In order to account for measurement and modelling errors, data noise was assumed to be proportional to prior data uncertainties σ_k^{prior}, and noise parameter λ (equation 3) was determined during the inversion. Uniform priors were given on the number of Voronoi cells as $[3, 4, ..., 100]$, on $\mu = \log(\rho)$ as $[-1, 5]$, on the x and z coordinates of model boundaries as $[-50, 50]$ and $[0, 30]$, respectively, and on noise parameter λ as $[0.01, 10]$. We ran 32 tempered Markov chains (of which 16 were at the target temperature $T_0 = 1$) in parallel for 6×10^5 iterations, allowing two randomly-chosen chains to swap models at each iteration provided the condition stated in equation 7 was satisfied. Every 100^{th} sample at the target temperature after a burn-in period of 2×10^5 iterations was considered as a representative model from the posterior PDF. This gave a solution to the inverse problem consisting of an ensemble of 64×10^3 samples $\mathbf{m} = [n, \mathbf{c}, \boldsymbol{\mu}, \mathbf{h}]$, where each parameter in $\mathbf{m}$ is distributed according to its posterior marginal PDF.

Information about the resistivity distribution in the subsurface may be visualised using histograms showing the marginal PDFs at a number of points in the xz plane (e.g., Figure 6) or by evaluating various statistics from the full PDF as described in Section 2.2.4. Some of these statistics are shown in Figure 7. Information on the resistivity of different subsurface structures can be obtained from the arithmetic mean, the median, the mode and the root-

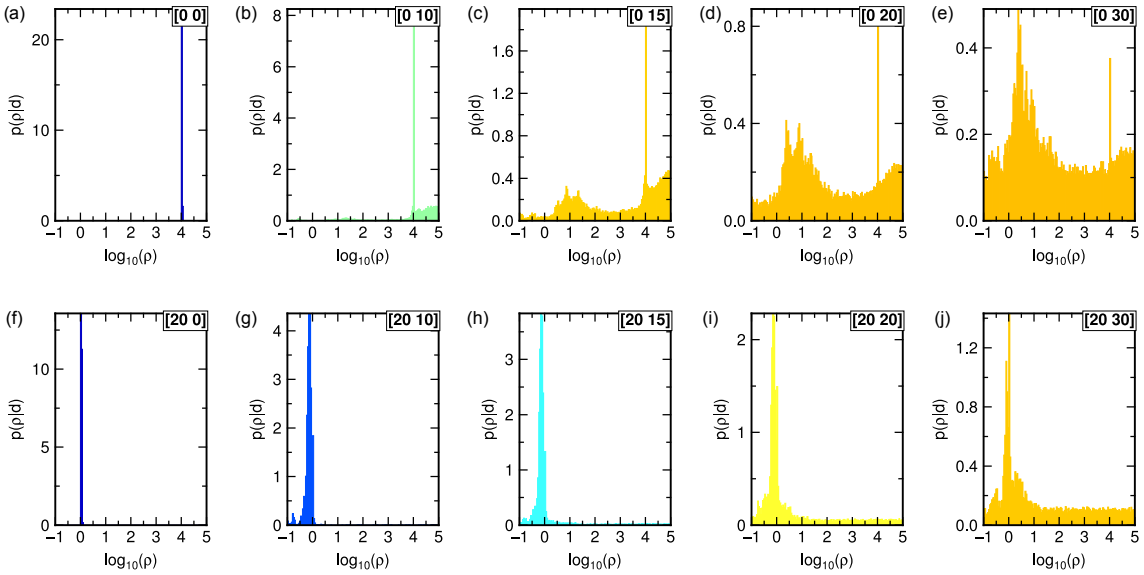

Figure 6. Posterior PDFs of $\log(\rho)$ at locations shown in Figure 5(a) estimated using the TERT algorithm. Posteriors in the top row are calculated at $x = 0$ m and (a) $z = 0$ m, (b) $z = 10$ m, (c) $z = 15$ m, (d) $z = 20$ m, (e) $z = 30$ m. Posteriors in the bottom row are calculated at $x = 20$ m and (f) $z = 0$ m, (g) $z = 10$ m, (h) $z = 15$ m, (i) $z = 20$ m, (j) $z = 30$ m. Histograms are colour-coded according to the standard deviation at their corresponding locations from Figure 7(e).

mean-square maps. While each single Voronoi model in the ensemble is discontinuous and unrealistic, each of these statistical measures provides a smoother representation of the true resistivity field and highlights specific features of the PDF across the imaged area. In addition, an impression of the *uncertainty* in our state of knowledge about the subsurface resistivity field may be obtained from the standard deviation and entropy maps, while skewness and excess kurtosis highlight information related to the *shape* of the PDF at each location in the xz plane. As previously noted in Section 2.2.4, none of these statistics can ever represent the complete solution to the inverse problem on their own, but should instead be interpreted together as part of a fully probabilistic solution.

As can be observed in Figures 7(a)–(d), the high-resistivity vertical structure in the centre of the model is resolved to varying degrees of accuracy to depths of between 10 m (arithmetic mean) and >20 m (mode, i.e., the maximum-a-posteriori value of every individual binned posterior resistivity pixel), while the background resistivity is generally resolved to larger depths (with the exception of the root-mean-square model). The standard deviation map in Figure 7(e) shows an increase in uncertainty vertically with increasing depth, and horizontally as the distance from the centre of the model increases. In fact, the increase in uncertainty with depth can also be observed on marginal PDFs along vertical profiles at $x = 0$ and $x = 20$ m (Figure 6): as depth increases, peaks in the PDF become less defined and the distribution approaches the Uniform prior (although still with peaks around the two values of log(resistivity) that appear in the true model in Figure 5). Similarly, excess kurtosis (Figure 7(f)) is positive in areas of low standard deviation indicating a more 'peaked' distribution, while it is negative in areas of high standard deviation when the posterior PDF approaches the Uniform prior.

In addition, the standard deviation plot in Figure 7(e) displays an increase in uncertainty along the vertical edge of the high-resistivity structure, showing that the exact shape and size of this body cannot be reconstructed. Indeed this high-uncertainty feature defines

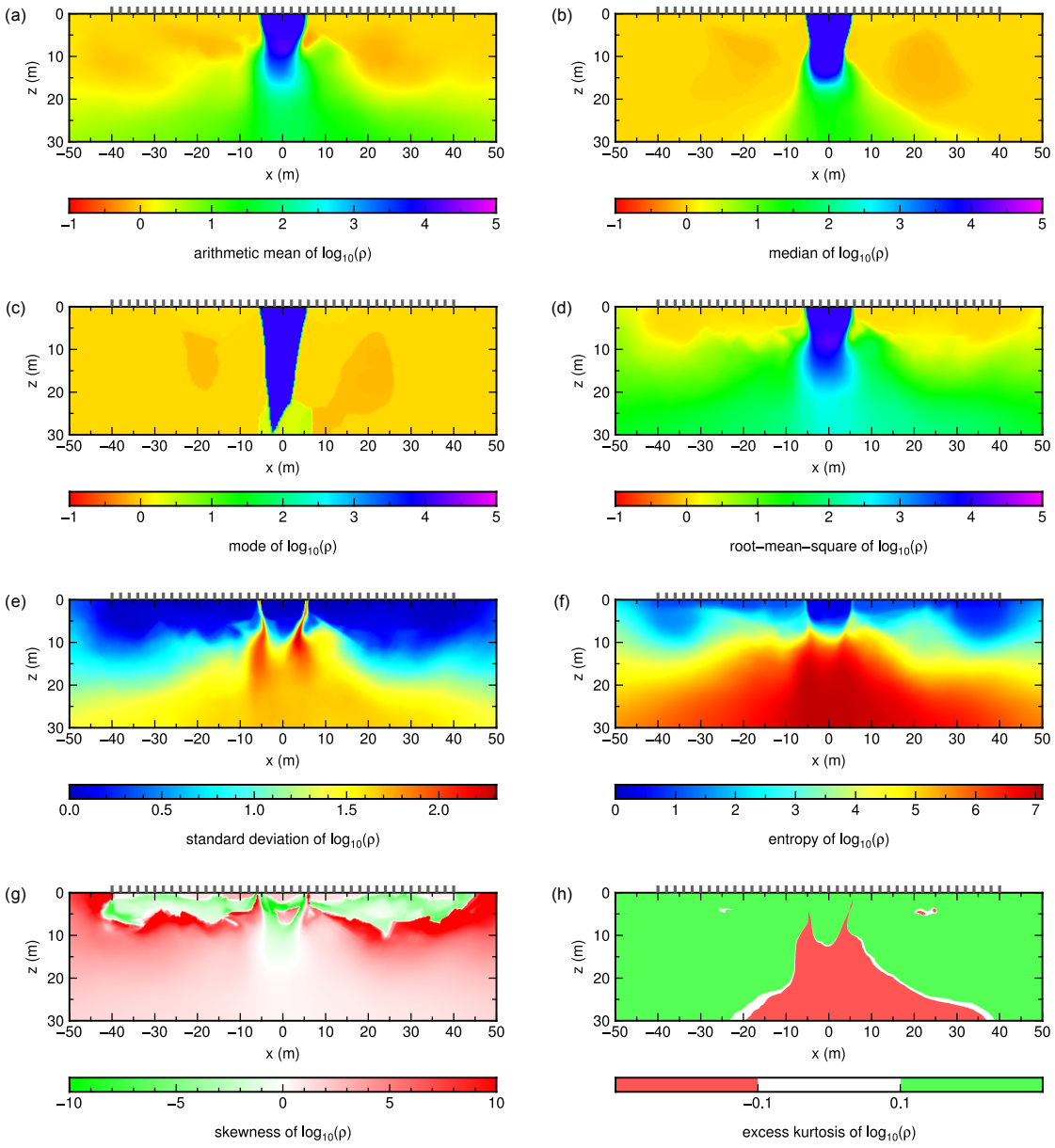

Figure 7. Inversion results for the synthetic model in Figure 5(a) found using the TERT algorithm. (a) Arithmetic mean. (b) Median. (c) Mode (i.e., maximum-a-posteriori). (d) Root-mean-square. (e) Standard deviation. (f) Entropy. (g) Skewness. (h) Excess kurtosis. Note that the excess kurtosis map is simplified to only 3 distinct groups of values due to the many orders of magnitude spanned by this statistical moment. In all panels, the grey ticks at $z = 0$ m denote electrode locations.

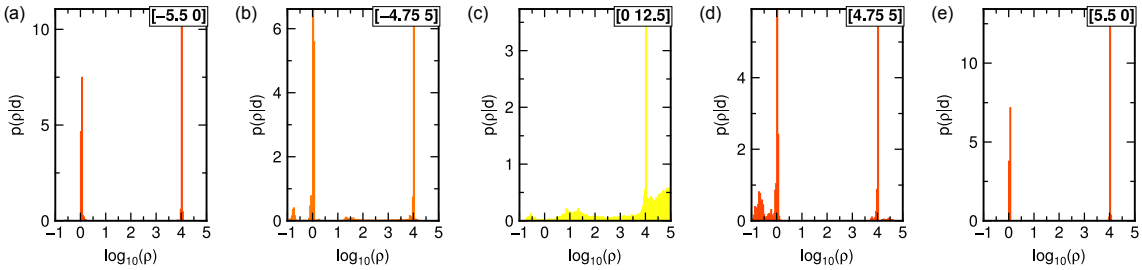

Figure 8. Posterior PDFs on $\log(\rho)$ for the synthetic model in Figure 5(a) found using the TERT algorithm. Posteriors are calculated at (a) $x = -5.5$ m and $z = 0$ m, (b) $x = -4.75$ m and $z = 5$ m, (c) $x = 0$ m and $z = 12.5$ m, (d) $x = 4.75$ m and $z = 5$ m, (e) $x = 5.5$ m and $z = 0$ m. Histograms are colour-coded according to the standard deviation at their corresponding locations from Figure 7(e).

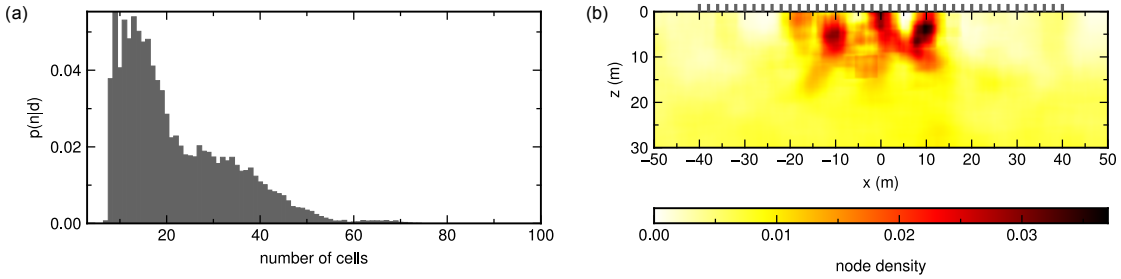

Figure 9. Information on the number of cells n in the posterior distribution and their locations found using the TERT algorithm. (a) Posterior PDF on the number of Voronoi cells ($p(n|\mathbf{d}^{obs})$). (b) Density of Voronoi nuclei across the ensemble of models in the PDF. At each pixel, density is measured within a 5 m × 5 m square sector centred on the pixel and is plotted as the average number of Voronoi nuclei per m^2 per sample. The grey ticks at $z = 0$ m in panel (b) denote electrode locations.

precisely the spatial resolution of this boundary, and its presence is independent of the electrode geometry employed since it occurs as a consequence of the true resistivity structure of the subsurface. Similar topologies have been observed in seismic traveltime tomography. Defined as 'uncertainty loops' by *Galetti et al.* [2015], they surround high- and low-velocity anomalies and characterise the uncertainty in the location of their boundaries. *Galetti et al.* [2015] conjectured that uncertainty loops should be observed in almost all tomographic systems provided that the full nonlinearity in the forward physics is embodied within the inversion, and that they may (erroneously) disappear in the solution of linearised systems. Loops have not previously been recognised in electrical resistivity tomography to the best of our knowledge, which may be because most publications employ inversion schemes involving linearised physics, or because those publications that do employ non-linearised, stochastic inversion methods fail to report uncertainty maps.

The origin of the loops is confirmed by the posterior PDFs on $\log(\rho)$ at points located near the edge of the high-resistivity anomaly (Figure 8): since these points may fall either inside or outside of the anomaly in the ensemble of accepted models, depending on exactly where the boundary of the anomaly is located in each model, their posterior PDFs are multimodal, and present two distinct peaks: one peak corresponds to the log(resistivity) of the anomaly while the other corresponds to the background log(resistivity). Excess kurtosis along the edges of the anomaly is also negative as a consequence of the distribution being bi-modal. The loops therefore appear because of our uncertainty in the geometrical location of the boundary of the anomaly, as embodied in the set of models in the ensemble.

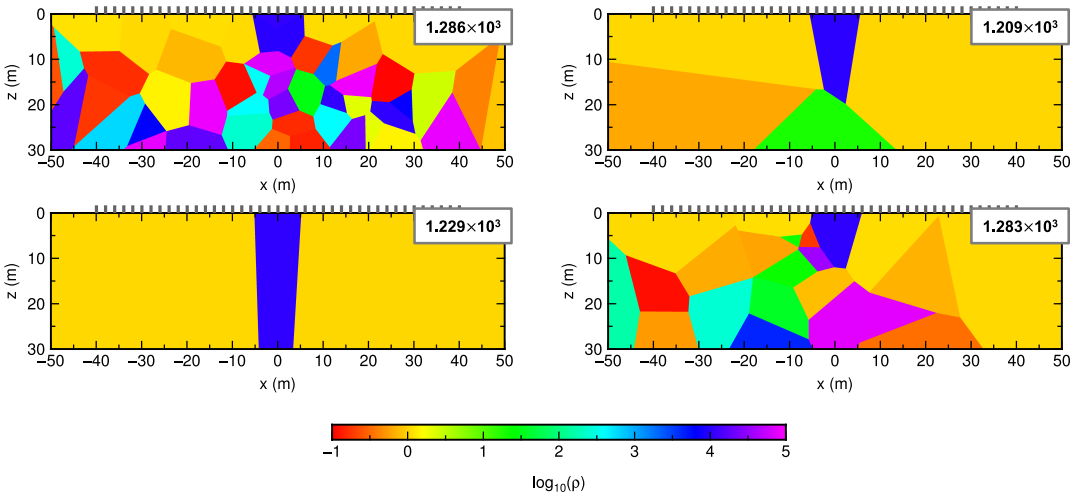

Figure 10. Example of 4 Voronoi models from the ensemble obtained from the TERT algorithm. The log-likelihood of each model is shown in the top-right corner of each plot. In all panels, the grey ticks at $z = 0$ m denote electrode locations.

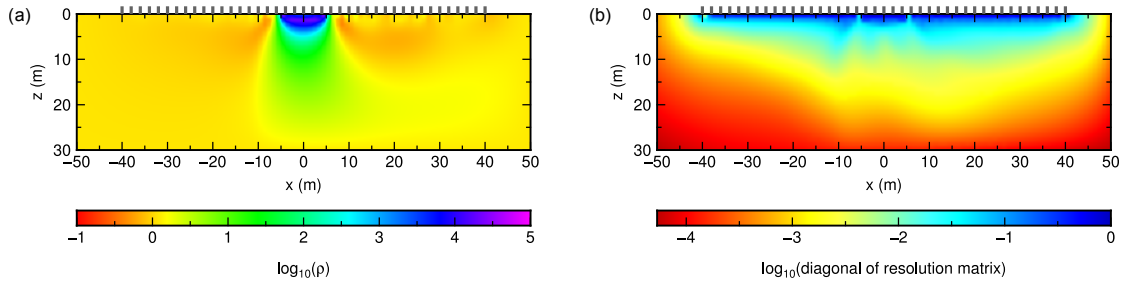

Figure 11. Inversion results for the synthetic model in Figure 5 found using the iterated-linearised code *R2* by *Binley* [2013b]. (a) Best-fit resistivity map obtained after 4 iterations. (b) Resolution map showing the logarithm of the diagonal elements of the resolution matrix (log values near 0 indicate better resolution). In both panels, the grey ticks at $z = 0$ m denote electrode locations.

In this transdimensional approach the number of model parameters n is itself a parameter. A posterior PDF is therefore also obtained on the number of Voronoi cells needed to constrain the data. The posterior $p(n|\mathbf{d}^{obs})$ is shown in Figure 9(a), while Figure 9(b) shows the density of Voronoi nuclei (given as average number of nuclei per m^2 per sample) in 5 m $\times$ 5 m square sectors centred on each pixel. As expected, the highest density of Voronoi nuclei is found near to the edges of the resistivity anomaly since this is the area in which the data is sufficient to resolve strongly heterogeneous structure which must be represented in almost any model in order to have a high enough likelihood to be included in the ensemble. However, although the structure of the true model is relatively simple and could easily be described by only 3 Voronoi cells (if the cell nuclei are located at specific positions), the posterior on the number of cells peaks around 14. This is likely to be due to the fact that this acquisition array has very low sensitivity to structure below 10 m depth, hence Voronoi cells may be added or deleted from the model below this depth without significantly affecting the likelihood. For instance, this is illustrated in Figure 10 which shows 4 different Voronoi models from the ensemble that, despite the different number of cells, have very similar likelihoods.

In order to benchmark the TERT algorithm against a standard optimisation-based inversion scheme, we inverted the same dataset using the iterative linearised code *R2* by *Binley* [2013b]. This code first uses a uniform resistivity model to estimate the data, and then iteratively adjusts the model until a target misfit value between observed and predicted data is reached. The resulting best-fit resistivity model obtained after 4 iterations is shown in Figure 11(a): although the background resistivity is correctly resolved across the model area, the high-resistivity structure in the middle of the model is only resolved down to $\sim$ 5 m, approximately half the depth to which it was observed in the arithmetic mean resistivity section from TERT (Figure 7(a)) and less than a quarter of that observed using the mode (Figure 7(c)). However, since a single best-fitting model is produced by the algorithm, it is not possible to evaluate the distance of the solution from the true model when that model is not known. The reliability of the solution in this optimisation inversion scheme must be assessed indirectly, for instance by analysing the resolution matrix $\mathbf{R}$ (e.g., see equation (5.18) in *Binley and Kemna* [2005]) computed using physics that is linearised around the model found in the final iteration. When $\mathbf{R}$ equals the identity matrix $\mathbf{I}$, all parameters are correctly resolved and uniquely determined; when $\mathbf{R}$ does not resemble the identity matrix, then each parameter is given by a weighted average of the true model parameters. The diagonal elements of the resolution matrix corresponding to the target misfit model in Figure 11(a) are shown in Figure 11(b). As expected from the acquisition geometry, resolution is higher (diagonal elements are closer to 1) near the surface and drops towards the bottom and lateral edges of the model. However, unlike the standard deviation map in Figure 7(e), the resolution matrix does not provide a range on the expected resistivities at any point in the model, hence it cannot be used as a direct measure of the uncertainty on the structures observed in Figure 11(a).

3.2 Example 2

In this second experiment, we created a synthetic dataset for the more complex resistivity model shown in Figure 12(a) using the forward modelling functions in *FW2_5D* and a dipole-dipole acquisition geometry (Figure 4(a)) with 41 electrodes located at regular intervals of 2 m. By letting the electrode spacing d vary between 2 and 26 m, and the dipole separation factor f vary between 1 and 6, we modelled 903 potential differences and perturbed each measurement k using random Gaussian noise with a standard deviation σ_k^{prior} of 3% of the observed value. The apparent resistivity pseudosection is shown in Figure 12(b). In this case, for a dipole-dipole electrode configuration, apparent resistivity is related to the measured potential difference ΔV_k by:

$$\rho_{app_k} = \pi d f(f+1)(f+2)\frac{\Delta V_k}{I_k} \tag{9}$$

We assume Uniform priors on the number of Voronoi cells as $[3, 4, ..., 100]$, on $\mu = \log(\rho)$ as $[-1, 5]$, on the x and z coordinates of model boundaries as $[-50, 50]$ and $[0, 30]$, respectively, and on noise parameter λ as $[0.01, 10]$, and ran 32 tempered Markov chains (of which 16 were at the target temperature $T_0 = 1$) in parallel for 1.2×10^6 iterations allowing two randomly-chosen chains to swap models at each iteration according to equation 7. Every 100^{th} sample at the target temperature after a burn-in period of 4×10^5 iterations was considered as a representative model from the posterior PDF, giving an ensemble of 128×10^3 valid samples.

Figures 13(a)–(d) map information retrieved by TERT about the distribution of resistivity in the subsurface in terms of different statistical moments. The background resistivity is relatively well resolved across the model, while the four rectangular anomalies are resolved to a different extent by the different statistics. The top two anomalies are resolved by all statistical moments in panels (a)–(d), while among the bottom two anomalies only the high-resistivity one on the right is resolved by all moments. The bottom low-resistivity anomaly is only visible as an area of slightly lower resistivity than the background in the median and mode maps, while it is not visible in the average and root-mean-square sections. This is not surprising given the higher sensitivity to larger values of these two statistical moments.

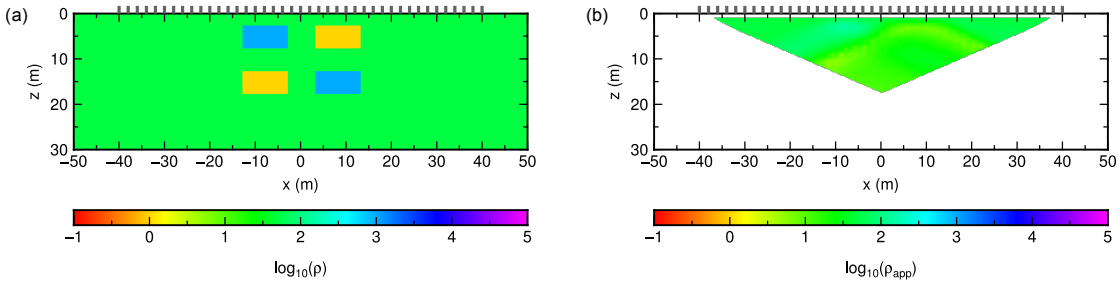

Figure 12. Synthetic resistivity model for the example application described in Section 3.2. (a) True resistivity section. (b) Resistivity pseudosection acquired using a dipole-dipole configuration for 41 electrodes located between -40 and 40 m, with electrode spacing d between 2 and 26 m and dipole separation factor f between 1 and 6 in the geometry shown in Figure 4(b). A resistivity pseudosection is a contour plot where each datum (i.e., apparent resistivity calculated using equation 9 for a dipole-dipole configuration) is plotted horizontally at the mid-point of the set of 4 electrodes used for the measurement, and vertically at the median depth of investigation [*Edwards*, 1977] of the electrode array used. In both panels, the grey ticks at $z = 0$ m denote electrode locations.

The uncertainty on the solution can be visualised on the standard deviation and entropy maps in panels (e)–(f). Similarly to the previous example, loops of higher standard deviation define the edges of the top two anomalies, and large values of standard deviation are also found vertically between the two sets of anomalies (around 10 m depth). Comparison of these high uncertainty features with the actual location of the anomalies' edges shows that the true edges fall within the high standard deviation loops, supporting our previous suggestion that these uncertainty topologies define the spatial resolution of boundaries between different bodies.

The skewness map shows areas of negative skewness corresponding to the two high resistivity anomalies, indicating that the tail of the PDF at these locations is longer on the low-resistivity side. On the other hand, the top low resistivity anomaly seems to correspond to an area of positive skewness, indicating that the PDF in this sector has a longer tail toward high resistivity values. This seems to agree with the fact that the background resistivity falls in between the resistivities of the low and high anomalies. The kurtosis map shows remarkable similarity to the entropy map, with areas of high entropy corresponding to areas of negative kurtosis. This is intuitively correct since negative kurtosis indicates flatter distributions, which in turn correspond to a greater degree of disorder or uncertainty as identified by entropy. In addition, a loop of negative kurtosis marks the edges of the top-left anomaly as a consequence of the posterior PDF being bi-modal in this region. However, it is important to note that both skewness and kurtosis maps may also be affected by the size of the prior, hence their interpretation should be treated with caution.

The least-misfit solution obtained using the linearised code *R2* is shown in Figure 14(a). In this case, only the top two anomalies are resolved, while the bottom two are not visible. In terms of assessing uncertainty, calculation of the resolution matrix $\mathbf{R}$ (which involves the inversion of a large matrix with rank equal to the number of model parameters, in this case 4032) was not possible computationally using *R2*. As a less computationally-intensive alternative, we calculated the sensitivity map $\mathbf{s}$ (see equation (5.20) in *Binley and Kemna* [2005]), which may be used instead of $\mathbf{R}$ as a less expensive image appraisal measure. Sensitivity is high in areas where the data is more strongly influenced by the model, while it is low in areas where the model has little effect on the data and hence may be mainly affected by the regularisation. However, note that using the sensitivity map to estimate uncertainty

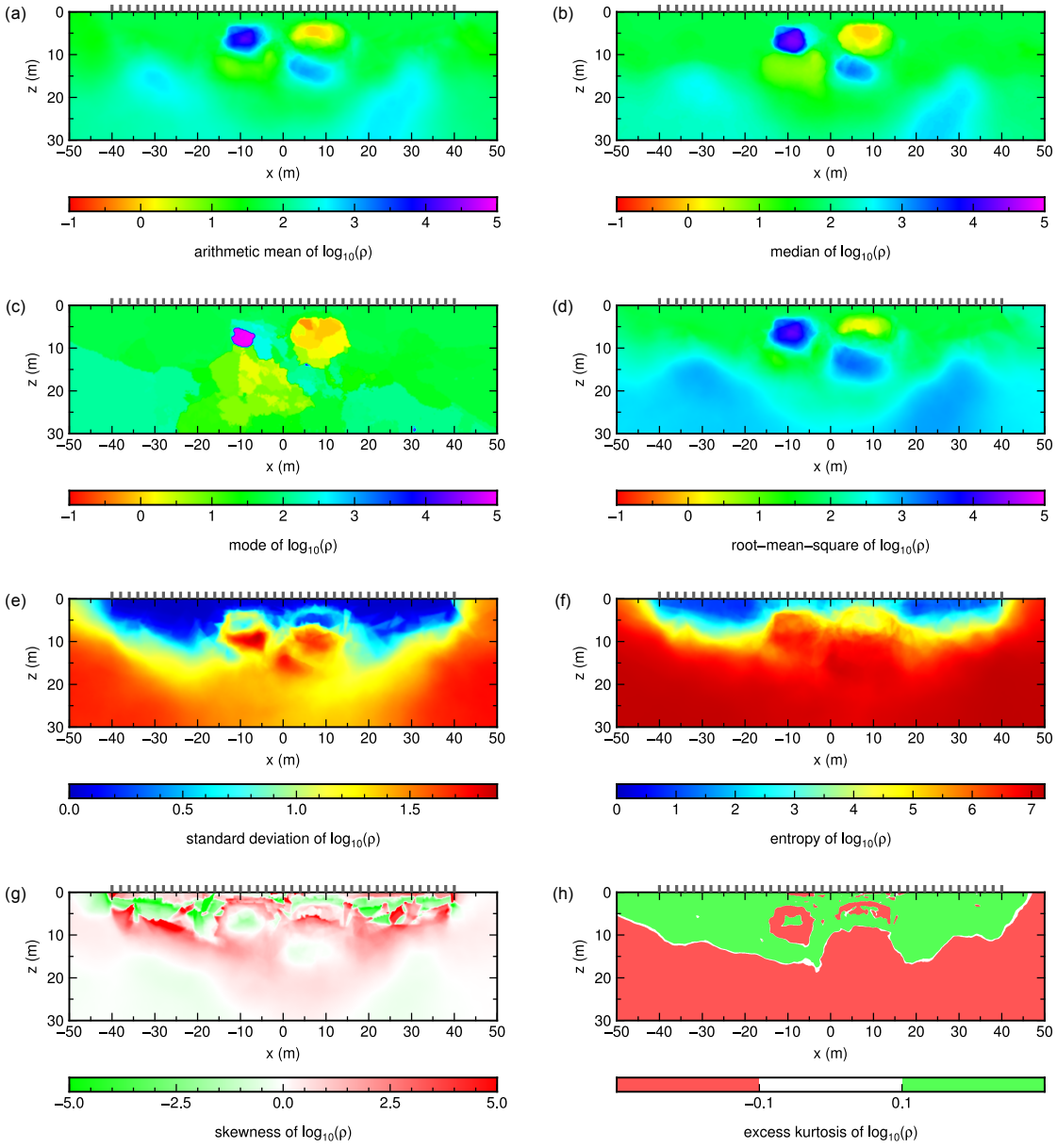

Figure 13. Inversion results for the synthetic model in Figure 12 found using the TERT algorithm. (a) Arithmetic mean. (b) Median. (c) Mode (i.e., maximum-a-posteriori). (d) Root-mean-square. (e) Standard deviation. (f) Entropy. (g) Skewness. (h) Excess kurtosis. Note that the excess kurtosis map is simplified to only 3 distinct groups of values due to the many orders of magnitude spanned by this statistical moment. In all panels, the grey ticks at $z = 0$ m denote electrode locations.

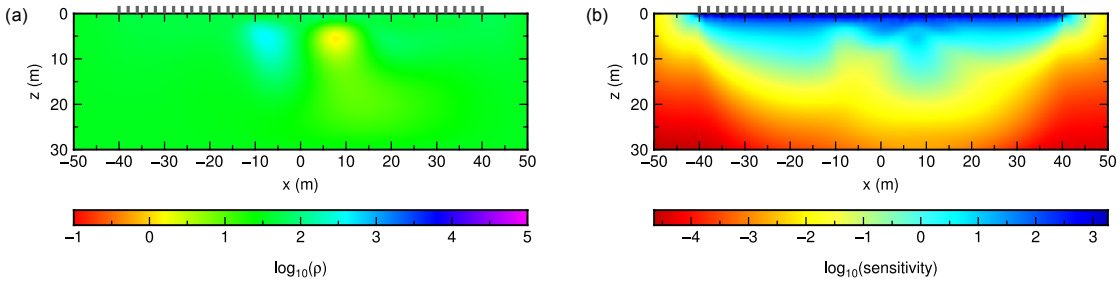

Figure 14. Inversion results for the synthetic model in Figure 12 found using the iterated-linearised code *R2* by *Binley* [2013b]. (a) Best-fit resistivity map obtained after 3 iterations. (b) Sensitivity map. In both panels, the grey ticks at $z = 0$ m denote electrode locations.

may be misleading in this case, since relatively high sensitivity is found at the location of the bottom-right, high-resistivity anomaly which is not resolved by the best-fit model.

4 Observational data experiments

In order to test the efficiency and reliability of the TERT method on observational data, we applied the method to two observational datasets acquired at archaeological sites in Scotland and Slovakia. The results from the Scotland dataset are presented below, while those from the Slovakia dataset are presented in the online Supporting Information.

4.1 Scotland dataset

In this experiment, we inverted two observational datasets recorded at an archaeological site at Glebe Field in Aberlady (Scotland). Glebe Field is listed as an officially Scheduled (protected) monument, and in recent years has yielded a number of Anglo-Saxon finds including small artefacts and coins. The site was also surveyed using magnetics [*Neighbour et al.*, 1995] and electrical resistance mapping [*Neighbour et al.*, 1998; *Blackwell*, 2008], revealing the presence of a number of linear features which were interpreted as building foundations. A resistance map (i.e., a standard archaeological twin-array output) obtained by *Blackwell* [2008] in the south-western corner of the field is shown in Figure 15.

We inverted two datasets recorded using a Wenner-alpha configuration along the two profiles shown in Figure 15: profile *A* (the green line in Figure 15) was acquired using 53 electrodes at 1 m spacing; profile *B* (the blue line in Figure 15) was acquired using 33 electrodes at 2 m spacing. Following an initial data quality check, the two profiles included 295 and 150 measured potential differences, respectively. We assumed data noise to be unknown, hence also inverted for parameters a and b in equation 4 in both cases.

We assumed Uniform priors on the number of Voronoi cells as $[5, 6, ..., 200]$, on $\mu = \log(\rho)$ as $[0.5, 4]$, and on noise parameters a as $[0.0001, 0.2001]$ and b as $[0.1, 1.1]$, respectively. Uniform priors on the x and z coordinates of model boundaries were assumed as $[-4, 56]$ and $[0, 16]$ for profile A, and as $[-4, 68]$ and $[0, 22]$ for profile B. We ran 32 tempered Markov chains (of which 16 were at the target temperature $T_0 = 1$) in parallel for 1×10^6 iterations allowing two randomly-chosen chains to swap models at each iteration according to equation 7. Every 100^{th} sample at the target temperature after a burn-in period of 2×10^5 iterations was considered as a representative model from the posterior PDF, giving an ensemble of 128×10^3 valid samples.

The results from the inversion using the TERT algorithm are shown in Figure 16(a)–(f), while panels (g) and (h) in Figure 16 show the inversion results obtained using the lin-

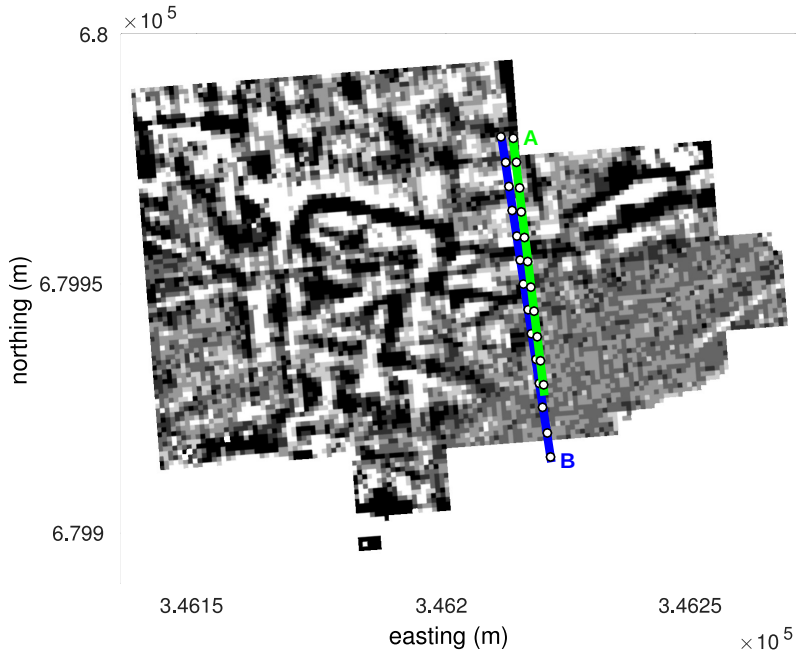

Figure 15. Resistance map of the south-west corner of Glebe Field, Aberlady (Scotland) by *Blackwell* [2008]. The two profiles for which imaging results are presented in Section 4.1 are denoted by the green (profile *A*) and blue (profile *B*) lines, where distance along the profile is measured from the northern end of the lines. The white circles on the two lines are for reference and denote 5-meter segments. Note that the location of the resistance map is approximate due to the original survey by *Blackwell* [2008] not being georeferenced.

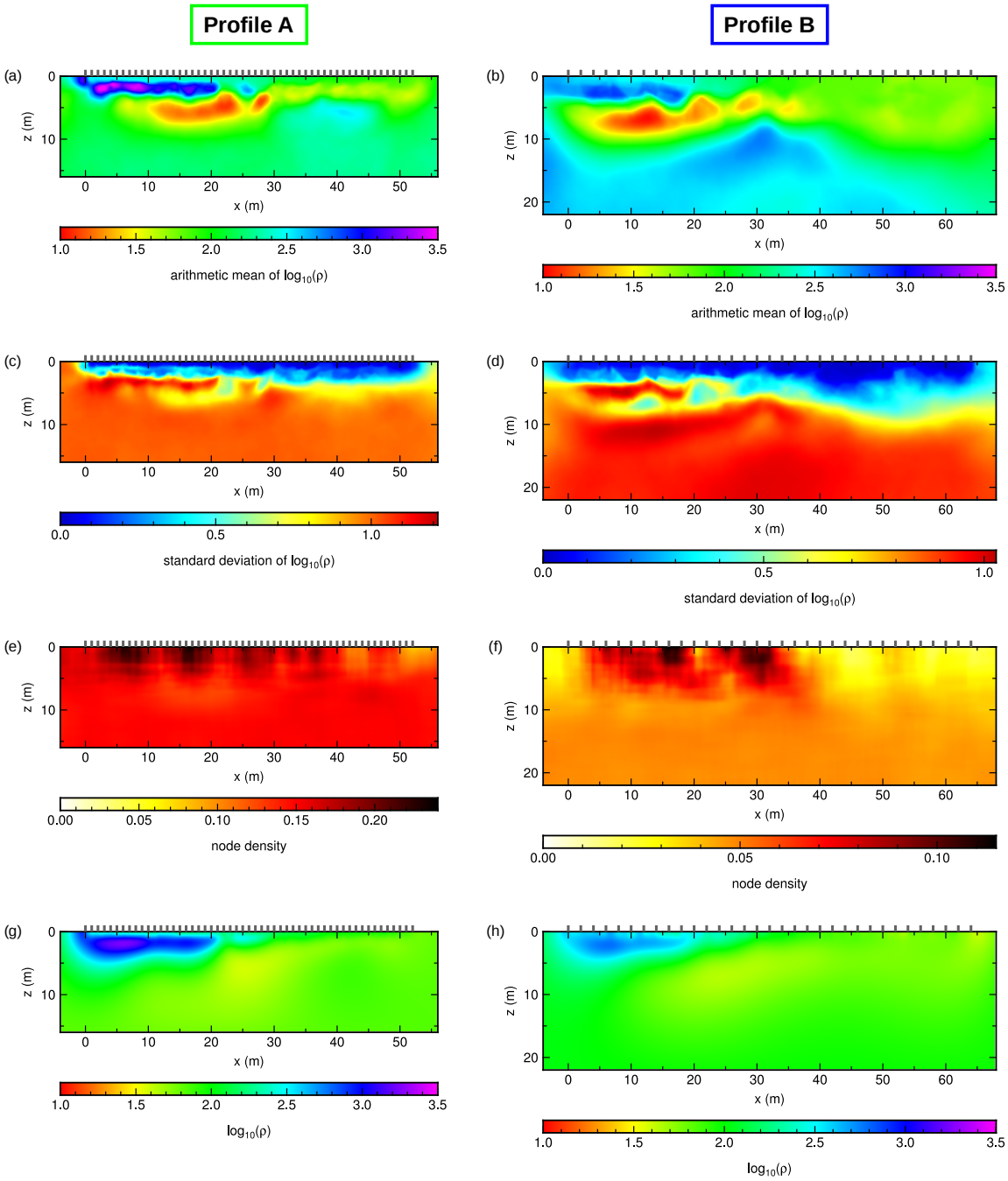

Figure 16. Inversion results for the observational datasets described in Section 4.1 found using (a)–(f) the TERT algorithm, and (g)–(h) the iterated-linearised code *R2* by *Binley* [2013b]. The left column shows results for profile A in Figure 15, the right column for profile B. (a)–(b) Arithmetic mean. (c)–(d) Standard deviation. (e)–(f) Node density (measured within a 5 m × 5 m square sector centred on each pixel). (g)–(h) Best-fit resistivity map from *R2*. Note that the colour scale in (a)–(b) and (g)–(h) is clipped between 1 and 3.5 to aid visualisation. In all panels, the grey ticks at $z = 0$ m denote electrode locations.

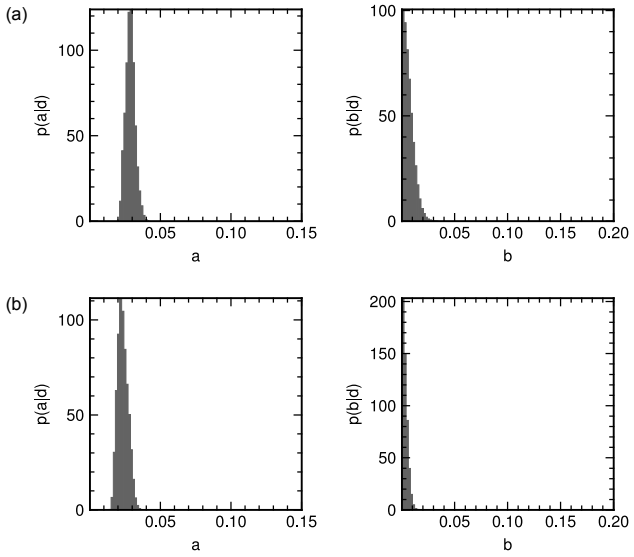

766 **Figure 17.** Posterior PDF on noise hyperparameters a and b for the observational dataset described in
767 Section 4.1 obtained from TERT. (a) Profile A. (b) Profile B.

763 earised code *R2*. The posterior on noise hyperparameters a and b are shown in Figure 17.
764 When inverting the data using *R2* the noise was assumed to be proportional to the measured
765 resistances according to equation 4, and a and b were set to 0.02 and 0.001, respectively.

768 In both profiles A and B, a high-resistivity structure is resolved near 2 m depth at the
769 northern end of the lines, and it is likely to correspond to buried paving from a building or
770 walkway. This feature appears to be thinner and better resolved in the average maps from
771 TERT compared to the linearised results from *R2*, probably as a result of smoothing in the
772 linearised solution.

773 In addition, the average maps from TERT reveal the presence of a high-resistivity
774 structure at depth (visible near $x = 40$ m and $z = 6$ m on profile A, and below $z = 10$ m
775 on profile B) which is not resolved at all in the linearised solution. This feature is located in a
776 region of high uncertainty and poor resolution as suggested by the standard deviation maps.
777 However, as shown by the synthetic example in Section 3.2, meaningful structure may still be
778 resolved by TERT in areas of high uncertainty (see the bottom-right anomaly in Figure 13),
779 hence it is not possible to tell whether this high-resistivity feature represents real structure or
780 an artefact from the inversion. Nevertheless, the fact that it is visible on both profiles A and
781 B seems to indicate that it is a robust feature which may represent resistive bedrock or some
782 other archaeological structure.

783 In terms of Voronoi cell density across the ensemble of valid models, similarly to the
784 previous example the highest density of Voronoi nuclei is found near the surface where reso-
785 lution is higher.

786 5 Discussion

787 5.1 Uninformative vs. informative priors

788 In all of the examples presented in this study we employed uninformative Uniform pri-
789 ors on all model parameters. This choice was mainly dictated by the fact that we wished to
790 assume little to no prior knowledge about the medium, and it prevented the emergence of

uncertainty loops and the increased depth resolution from being in any sense confounded between the information contained in the priors and in the data.

However, were more detailed prior information available in the form of alternative surveys or boreholes, such information could be included within the inversion in terms of informative priors. The use of Voronoi cells to represent the model creates a very flexible type of model parameterisation, and such cells could easily provide approximate representations of both such prior information and the resulting posteriors: if prior information were both strong (permitting only tightly constrained, geologically-realistic structures) and detailed, then the number of cells may increase to reflect that level of detail; in contrast, in the absence of strong priors, Voronoi cells would provide a lower-dimensional, more approximate representation of the geology – to the extent that the geology would be reflected in the ERT data alone during inversion.

Alternatively, linearised inversion starting from different initial models might be used to produce a set of solutions which may then be used as starting points for non-linear inversion using TERT (with each Markov chain or a set of Markov chains using a different linearised solution as an initial model). If the linearised solutions are significantly different, this 'hybrid' method might allow convergence to be reached more quickly.

While we have not implemented either of the two approaches suggested above, we believe they would provide an interesting topic for further research.

5.2 Convergence

In any McMC inversion scheme it is important to collect a sufficient number of samples so that the ensemble of sampled models will be reasonably representative of the posterior PDF. If a Markov chain could be run for an infinite amount of time, it would explore the full model space and reach convergence in the region of highest probability. However, since computational limitations impose a practical limit on the running time of the inversion, convergence may not be reached by the end of the chain if it gets trapped in a local likelihood maximum. A practical solution to this problem is to run a series of Markov chains in parallel by starting from different initial conditions. This ensures that different regions of the model space can be explored simultaneously, and that anomalous Markov chains that are stuck in a local likelihood maximum can easily be identified.

Although few tools are currently available for assessing convergence in a transdimensional framework, information on Markov chain convergence may be obtained by plotting the variation of a model parameter as a function of iteration. However, as opposed to traditional McMC methods where model parameterisation is fixed, in a rj-McMC tomography scheme the use of cell position and log(resistivity) values ($\mathbf{c}$, μ) to assess convergence is pointless since the dimensionality of the geometry of the model may change at each step of the chain. Instead, useful convergence diagnostics may be obtained from plots of number of cells, noise hyperparameters, or log(resistivity) at a certain location versus iteration number. Convergence of one of these parameters may be said to have been reached when its value becomes relatively stationary and no drifts are present as the parameter is plotted as a function of sample number.

One of the main factors affecting the speed at which convergence is reached is the choice of the perturbation step sizes (see Appendix B.3 for a detailed description of these terms). In order to promote convergence and prevent biases in the evaluated posterior PDF, the shape of the proposal distribution from which each proposed model is drawn should be as similar as possible to that of the posterior PDF. However, this is problematic given that the shape of the posterior is not known *a priori*. Hence, as expressed in equation B.12, the proposal distribution for $\mathbf{m}'$ is chosen to be conditionally dependent on the current model $\mathbf{m}$, so that the proposed model is simply a perturbation of $\mathbf{m}$ whose magnitude is determined by the step size. Suitable step sizes are normally chosen through trial and error by analysing

the acceptance rates (i.e., number of accepted samples over number of proposed samples) for the various types of perturbation, and a number of authors have suggested acceptance rates of around 1/4 for optimal sampling [*Gelman et al.*, 1996; *Sherlock and Roberts*, 2009]. If a certain acceptance rate is too low, the step size of the perturbation is likely to be too large as the proposed models fall either in regions of lower probability or outside of the prior bounds. If the acceptance rate is too high, then the proposed models are likely to be too close to the current models, causing the algorithm to explore only a small portion of the model space and slowing down convergence.

However, monitoring acceptance rates and manually tuning step sizes during a number of test runs may be cumbersome and computationally prohibitive due to the large computational cost of the inversion (see Section 5.3). Similarly to *Bodin and Sambridge* [2009], we overcome this issue for non-transdimensional steps by implementing the 'delayed rejection' scheme of *Tierney and Mira* [1999], which allows a second proposal on the value or position of Voronoi nuclei to be made by using a smaller step size if the first proposal is rejected. While this appears to improve the acceptance of *resistivity* and *move* steps, we find that the acceptance rates of transdimensional steps (birth and death) are normally very low ($< 10\%$). Hence, a natural extension of this study might include attempting to improve the acceptance rates of transdimensional steps by implementing a 'transdimensional delayed rejection' scheme as developed by *Green and Mira* [2001], and/or by sampling the log(resistivity) value for newly-generated Voronoi cells from the prior rather than using a Gaussian perturbation (equation B.16) as suggested by *Dosso et al.* [2014].

The choice of the prior also plays a role on Markov chain convergence, with wider priors normally causing convergence to be slower. This is intuitive since, for the same Markov chain length, wider prior boundaries imply that a larger portion of model space must be explored. Hence, although the use of a wider prior ensures that fewer prior-related biases are introduced into the solution, it also means that Markov chains need to be run for a longer time in order to reach convergence. A compromise between prior width and practicality must therefore sometimes be made given the limitations on the available computing time (even though this violates a strictly Bayesian approach where the prior should be independent of the current data and inversion algorithm).

The fit to the observed data may be estimated by calculating the residuals obtained from each Voronoi model within the ensemble, which for the examples considered in this paper are shown in Figure 18 as a percentage of the observed potential differences. In all cases, the distribution of the residuals resembles a Gaussian distribution and is centered around 0.

5.3 Computational cost

We initially implemented the TERT algorithm in MATLAB since it allowed for rapid testing, modification and debugging. In addition, given that the resistivity modelling code *FW2_5D* by *Pidlisecky and Knight* [2008] which we employed is freely available as a suite of MATLAB functions, implementation in MATLAB allowed us to make use of a thoroughly tested and, to the best of our knowledge, error-free forward modeller. However, despite the use of the Parallel Computing MATLAB Toolbox, executing inversions in MATLAB required a substantial amount of computation time, hence we re-wrote our program entirely in Fortran after the initial testing stage. This gave us a considerable gain in computation time (around 1/3 time required for an inversion) and allowed us to leverage the resources of a computing cluster by using parallel computing tools such as MPI in the inversion algorithm. As an example, in its current Fortran implementation the running time of the code for the electrode geometries discussed in Section 3 is on average 4 hours for 10^4 iterations, using 32 cores for 32 parallel Markov chains on the cluster at the University of Edinburgh. Further reductions in computation time could be made in future by also parallelising the forward modelling routines.

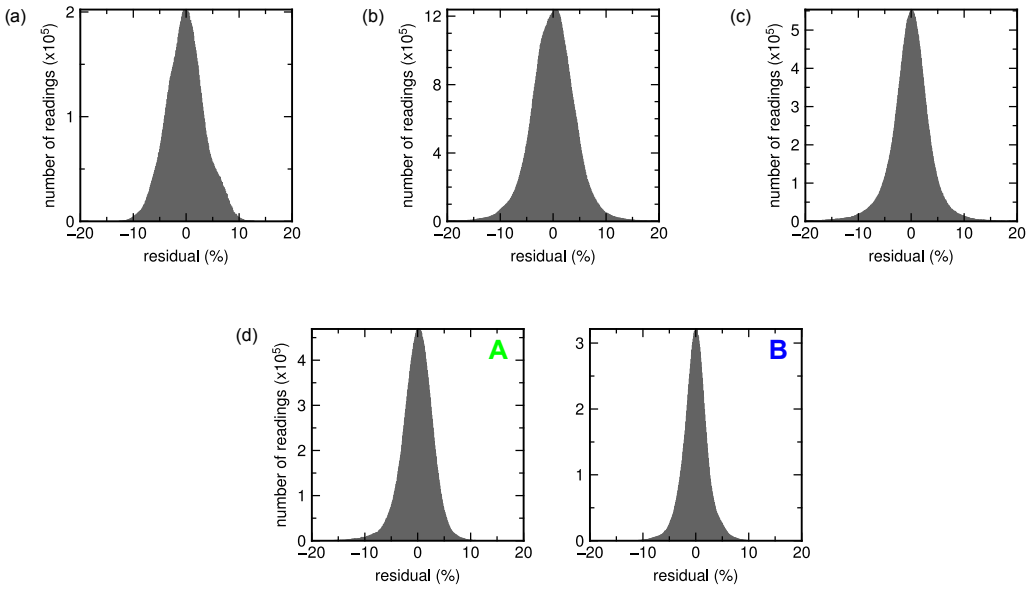

Figure 18. Residuals as percentage of the measured data evaluated for each Voronoi model in the ensembles obtained for the examples described in (a) Section 3.1, (b) Section 3.2, (c) Section 1 of the Supporting Information, (d) Section 4.1 (profile *A* on the left, profile *B* on the right).

In terms of its applications, while TERT is computationally expensive in its current implementation, it is nevertheless applicable to the monitoring of higher-value targets where larger cost is acceptable. Examples include the detection and monitoring of leaks from nuclear waste storage sites, or monitoring CO_2 plumes which might escape from subsurface storage reservoirs through chimney structures.

5.4 A note on natural parsimony

As described earlier, the rj-McMC algorithm provides a naturally parsimonious way of performing tomography in that among models giving similar data fit, simpler ones (i.e., those with fewer Voronoi cells) are assigned higher probability. This becomes obvious when Bayes' theorem (equation 2) is analysed together with the prior function in equation B.11, which decreases exponentially as the number of cells n increases (Figure B.1).

However, the concept of natural parsimony is not as straightforward to grasp when we consider the Metropolis-Hastings algorithm (which we employ to draw samples from the posterior PDF) since the number of cells n does not explicitly appear in any of the expressions for the acceptance parameter $\alpha(\mathbf{m}'|\mathbf{m})$ when a change in model dimension is involved (equations B.26 and B.27). In order to gain more intuition on the concept of natural parsimony, let us analyse equations B.26 and B.27 in more detail.

As described in Section 2.2.4, a proposed model $\mathbf{m}'$ is accepted if $\alpha(\mathbf{m}'|\mathbf{m}) \geq r$, where r is a random deviate from a Uniform distribution between 0 and 1, while it is randomly accepted or rejected if $\alpha(\mathbf{m}'|\mathbf{m}) < r$. This selection criterion ensures that all samples that improve the data fit are accepted, while also allowing lower-probability regions in the model space to be explored.

In the case of perturbation types of *fixed* dimensionality (i.e., changing resistivity or noise, or moving a Voronoi nucleus), the acceptance parameter $\alpha(\mathbf{m}'|\mathbf{m})$ only depends on the likelihoods of the current and proposed models (equation B.25), and the proposed model $\mathbf{m}'$

is always accepted if its likelihood is greater than that of the current model $\mathbf{m}$. In the case of birth and death steps, however, the acceptance parameter $\alpha(\mathbf{m}'|\mathbf{m})$ depends not only on the likelihoods of $\mathbf{m}$ and $\mathbf{m}'$, but also on a number of other parameters such as the standard deviation of the step size σ_{bd}, the prior probability of log(resistivity) $\Delta\mu$, and the difference in log(resistivity) between the current and proposed model at the location where a Voronoi nucleus is added or removed (equations B.26–B.27). As a result, in order for a birth/death step to be definitely accepted, the term in the square brackets of equation B.26/B.27 must be greater than or equal to 1 (or, equivalently, its logarithm must be greater than or equal to 0). By taking the natural logarithm of this term, setting it equal to or greater than 0, and rearranging the terms, we obtain

$$\psi(\mathbf{m}) - \psi(\mathbf{m}') \geq -2 \times \left[\ln\left(\frac{\sigma_{bd}\sqrt{2\pi}}{\Delta\mu} \right) + \frac{(\mu'_{n+1} - \mu_i)^2}{2\sigma_{bd}^2} \right] \tag{10}$$

in case of a birth step, and

$$\psi(\mathbf{m}) - \psi(\mathbf{m}') \geq -2 \times \left[\ln\left(\frac{\Delta\mu}{\sigma_{bd}\sqrt{2\pi}} \right) - \frac{(\mu'_j - \mu_i)^2}{2\sigma_{bd}^2} \right] \tag{11}$$

in case of a death step, where $\mu = \log(\rho)$, $\psi(\mathbf{m})$ and $\psi(\mathbf{m}')$ denote the data misfit (defined in equation B.2) of the present and proposed model, σ_{bd} is the proposal step size for birth and death steps, ln denotes the logarithm in base e, and for simplicity we have assumed data noise to be constant between model $\mathbf{m}$ and $\mathbf{m}'$ (i.e., $\sigma_k = \sigma'_k$ in equations B.26–B.27).

Equations 10 and 11 illustrate how, for a birth or death step to be definitely accepted, the difference in misfit between the current and the proposed model ($\psi(\mathbf{m}) - \psi(\mathbf{m}')$) must be greater than or equal to the quantity on the right-hand-side of each equation, while the model is randomly accepted or rejected if the difference in misfit is less than this quantity (see Section 2.2.4). The right-hand-side of equations 10 and 11 is displayed in Figure 19 as a function of the change in log(resistivity), $\delta\mu$, between the proposed and current model (where $\delta\mu = |\mu'_{n+1} - \mu_i|$ in a birth step, and $\delta\mu = |\mu'_j - \mu_i|$ in a death step), using the same prior and step size as in the synthetic examples from Section 3. The two curves in Figure 19 cross at

$$\delta\mu_0 = \sigma_{bd}\sqrt{2 \times \ln\left(\frac{\Delta\mu}{\sigma_{bd}\sqrt{2\pi}} \right)} \tag{12}$$

This value is important as it separates the values of $\delta\mu$ for which there are expected to be more death steps than birth steps (to the left of this value) from those for which the reverse is true (to the right). This value varies with the proposal step size σ_{bd} and peaks at

$$\sigma_{bd}^{max} = \frac{\Delta\mu}{\sqrt{2\pi}} \mathrm{e}^{-1/2} \tag{13}$$

For simplicity, let us refer to the area of the plot in Figure 19 located to the left of $\delta\mu_0$ as the region where the change in the model is small, and the region to the right of $\delta\mu_0$ as the region where the change in the model is large.

When the change in the model is small, all death steps which decrease the misfit (even by a very small amount) are accepted, while birth steps are only definitely accepted if model $\mathbf{m}'$ yields a significantly lower misfit than the current model. This ensures that an increase in model dimensions is justified by a substantial decrease in misfit from $\mathbf{m}$ to $\mathbf{m}'$ if the two models are similar, and that the number of model dimensions always decreases if accompanied by an improvement in data fit – according to the principles of natural parsimony. However, note that, in practical applications, the acceptance rate of birth steps is normally found to be low when the step size σ_{bd} is very small, since it is unlikely that the decrease in misfit will be large enough for small model perturbations.

When the change in the model is large, birth steps are always accepted if they improve the data fit, while death steps must yield a substantial improvement in fit in order to be definitely accepted. Although this appears to be against the principles of natural parsimony, note

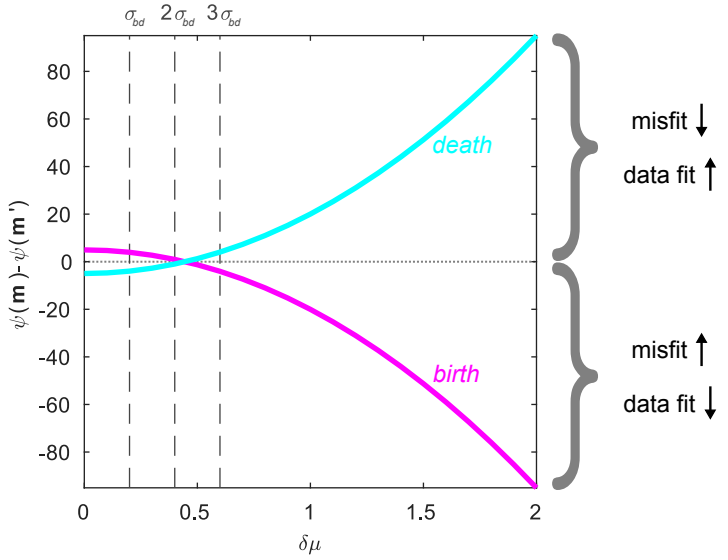

Figure 19. Difference in misfit between current model $\mathbf{m}$ and proposed model $\mathbf{m}'$ as a function of change in log(resistivity), $\delta\mu$ (where $\delta\mu = |\mu'_{n+1} - \mu_i|$ in a birth step, and $\delta\mu = |\mu'_j - \mu_i|$ in a death step), calculated using equations 10 (birth, purple line) and 11 (death, light blue line), and the prior parameters from the synthetic examples in Section 3. Model $\mathbf{m}'$ is always accepted if the difference in misfit $\psi(\mathbf{m}) - \psi(\mathbf{m}')$ lies above the purple line for a birth step and above the light blue line for a death step, and randomly accepted or rejected otherwise. The vertical dashed lines indicate the values below which $\delta\mu$ is likely to fall with probability 68.27% (at σ_{bd}), 95.45% (at $2\sigma_{bd}$) and 99.73% (at $3\sigma_{bd}$).

that the majority of the time the change in log(resistivity), $\delta\mu$, will be less than σ_{bd}, which is assumed to be significantly less than the prior range of log(resistivity), $\Delta\mu$. In fact, because the proposal distributions for birth and death steps are Gaussian, $\delta\mu$ has a probability of around 68%, 95% and 99.7% of falling respectively within one, two and three standard deviations σ_{bd} from μ_i, as displayed by the vertical dashed lines in Figure 19.

Similarly to Figure 19, the right-hand-side of equations 10 and 11 for different values of σ_{bd} is displayed in Figure 20. As σ_{bd} increases, the crossing point $\delta\mu_0$ moves to the right (panels (a)–(c)) (extending the region of naturally parsimonious proposals to the right) up to $\sigma_{bd} = \sigma_{bd}^{max}$ in panel (c). The crossing point $\delta\mu_0$ moves back to the left for $\sigma_{bd} > \sigma_{bd}^{max}$ (panels (d)–(e)), and the two curves cross at $\delta\mu_0 = 0$ when $\sigma_{bd} = \Delta\mu/\sqrt{2\pi}$ (panel (e)). Beyond this value all birth steps that improve the data fit are accepted, while only death steps that provide a substantial decrease in misfit are always accepted (panel (f)).

Clearly the latter case is not parsimonious as birth steps are likely to exceed death steps (and $\delta\mu$ would be so large that either μ'_{n+1} would fall outside the prior support or model $\mathbf{m}'$ could not be considered 'similar' to model $\mathbf{m}$ as required by natural parsimony), and hence this places a bound on reasonable values of σ_{bd}. Plots such as those shown in Figure 20 may therefore be used to choose an appropriate value for σ_{bd}, such that the crossing point of the two curves is greater than 1 or 2 standard deviations from μ_i, ensuring that natural parsimony will be achieved on average. Alternatively, the resistivity of a newly-generated cell in a birth step may be sampled from the prior as suggested by *Dosso et al.* [2014], which obviates the need for such tuning when prior ranges are narrow.

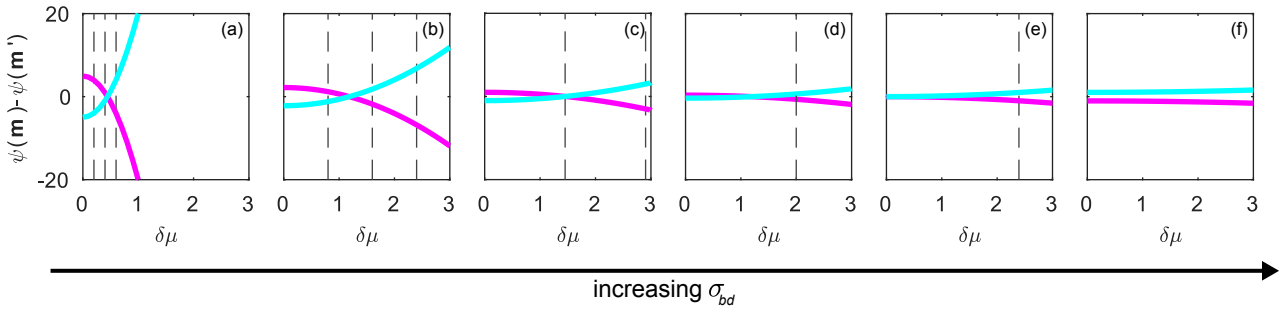

Figure 20. Difference in misfit between current model $\mathbf{m}$ and proposed model $\mathbf{m}'$ as a function of change in log(resistivity) $\delta\mu$ (where $\delta\mu = |\mu'_{n+1} - \mu_i|$ in a birth step, and $\delta\mu = |\mu'_j - \mu_i|$ in a death step), calculated using equations 10 (birth, purple line) and 11 (death, light blue line), the prior on log(resistivity) from the synthetic examples in Section 3, and different proposal sizes σ_{bd}: (a) 0.2, (b) 0.8, (c) 1.4518 (i.e., σ_{bd}^{max} as given in equation 13), (d) 2, (e) 2.3937 (i.e., $\Delta\mu/\sqrt{2\pi}$), (f) 4. Where visible, the vertical dashed lines denote $\delta\mu$ equal to σ_{bd}, $2\sigma_{bd}$ and $3\sigma_{bd}$ as in Figure 19.

6 Conclusions

We have described a method for electrical resistivity tomography which uses the reversible-jump Markov chain Monte Carlo algorithm and model parameterisation with Voronoi cells to produce an ensemble of solutions to the inverse problem which are distributed according to the posterior probability density function. The advantage of this approach lies in the fact that, by never linearising the physics of the forward modelling problem and allowing the model parameterisation to vary freely during inversion, we reduce both modelling- and parameterisation-related biases to a minimum while efficiently exploring the model space. In addition, since no actual matrix inversion is involved in the inversion process, this method obviates the need for any user-defined regularisation – the variation and smoothness of the solution is constrained by noise in the data. More importantly, both synthetic and observational examples showed that depth resolution increases when non-linearities are correctly accounted for during the inversion.

Each of the models in the ensemble solution is defined by a tessellation of Voronoi cells with different resistivity. While each of these models is unrealistic when taken on its own, the full ensemble of solutions provides a probabilistic representation of subsurface resistivity structures and of their uncertainties. Statistical moments such as the arithmetic mean, the harmonic mean, the median, the mode and the root-mean-square can be computed through the ensemble to obtain a visual representation of the subsurface resistivity field. Each of these moments is sensitive to different properties of the ensemble (see Section B.5 in the Appendix) and, despite the discontinuous nature of the underlying Voronoi models, provides a smooth representation of subsurface resistivity.

In addition, compared to an optimisation approach, a sampling-based probabilistic solution has the inherent advantage that uncertainties can be directly evaluated from the posterior probability density function. Within this paper, we considered standard deviation and entropy as measures of uncertainty, and found that their magnitude is not only dictated by the resolution provided by the data, but also by the true underlying resistivity structure. In fact, both synthetic and observational data examples showed that the density of Voronoi nuclei is greater where the variability of the true resistivity field is larger and where structures are of smaller scale.

A: Forward modelling

The flow of electrical current in the Earth's subsurface is governed by Ohm's law, which states that at each point the current density $\mathbf{J}$ is directly proportional to the electric field intensity $\mathbf{E}$ and inversely proportional to the resistivity of the medium ρ:

$$\mathbf{J} = \frac{1}{\rho}\mathbf{E} \tag{A.1}$$

If the electric field $\mathbf{E}$ is stationary in time, it can be expressed in terms of a scalar potential Φ as

$$\mathbf{E} = -\nabla\Phi \tag{A.2}$$

which allows us to re-write equation A.1 as

$$\mathbf{J} = -\frac{1}{\rho}\nabla\Phi \tag{A.3}$$

By the principle of conservation of charge and the equation of continuity, we obtain the following expression,

$$\nabla \cdot \mathbf{J} = \frac{\partial q}{\partial t}\,\delta(\mathbf{x} - \mathbf{x}_S) \tag{A.4}$$

where $\mathbf{x}_S$ is the location of a point source of charge density q, and $\delta(\mathbf{x} - \mathbf{x}_S)$ is the Dirac delta function centred at the current source location $\mathbf{x}_S$. By combining equations A.3 and A.4, and expressing current I as the change of charge density over time ($I = \partial q/\partial t$), we obtain the domain equation [*Dey and Morrison*, 1979a,b; *Pridmore et al.*, 1981]

$$\nabla \cdot \left[\frac{1}{\rho(\mathbf{x})}\,\nabla\Phi(\mathbf{x})\right] = -I\,\delta(\mathbf{x} - \mathbf{x}_S) \tag{A.5}$$

which describes the distribution of the electrical potential generated by a point source of electrical current at location $\mathbf{x}_S$. Solving this equation to determine the potential Φ which is generated by the injection of electrical current from an electrode located at $\mathbf{x}_S$ and observed at $\mathbf{x}$, given a certain distribution of resistivity $\rho(\mathbf{x})$ in the subsurface, corresponds to most of the *forward* problem. The data usually recorded in ERT are differences in the electrical potential at pairs of locations; calculating these differences for the potential Φ completes the forward problem.

B: Mathematical details for the rj-McMC algorithm

B.1 The likelihood

The likelihood function $p(\mathbf{d}^{obs}|\mathbf{m})$ can be thought of as a measure of the misfit between observed and predicted data. Using a Gaussian distribution to represent data uncertainty, the likelihood function can be expressed as

$$p(\mathbf{d}^{obs}|\mathbf{m}) = \frac{1}{\sqrt{(2\pi)^K |\mathbf{C}_d|}}\,\exp\left\{-\frac{1}{2}\,(\mathbf{d}^{obs} - \mathbf{d}^{pred})^{\mathrm{T}}\,\mathbf{C}_d^{-1}\,(\mathbf{d}^{obs} - \mathbf{d}^{pred})\right\} \tag{B.1}$$

where $\mathbf{d}^{pred} = \mathbf{g}(\mathbf{m})$, $\mathbf{C}_d$ is the data covariance matrix and $|\mathbf{C}_d|$ represents its determinant.

If data noise is uncorrelated, $\mathbf{C}_d$ in equation B.1 is a diagonal matrix whose elements are the variances (i.e., squared standard deviations) of the data uncertainties. The data misfit function $\psi(\mathbf{m})$ can then be defined using the L_2 norm (chi-squared error) as

$$\psi(\mathbf{m}) = \sum_{k=1}^{K}\left(\frac{d_k^{obs} - d_k^{pred}}{\sigma_k}\right)^2 \tag{B.2}$$

where K represents the total number of data points, d_k^{pred} is the k^{th} datum predicted from model $\mathbf{m}$, and σ_k is the standard deviation of the uncertainty associated with datum d_k^{obs}. Combining equations B.1 and B.2 yields

$$p(\mathbf{d}^{obs}|\mathbf{m}) = \frac{1}{\prod_{k=1}^{K}\left(\sqrt{2\pi}\,\sigma_k\right)}\,\mathrm{e}^{-\psi(\mathbf{m})/2} \tag{B.3}$$

B.2 The prior

Since all inferences about the posterior PDF are relative to the prior distribution, priors have great importance in Bayesian inversion schemes as the final result may be heavily influenced by the choice of an inappropriate prior. In order to minimise the contribution of prior-related biases that are introduced into the solution, we choose Uniform prior distributions with wide bounds for all model parameters in the examples herein. Given that all parameters are independent and have different dimensions, the model prior can then be divided into the product of four terms:

$$p(\mathbf{m}) = p(n)\; p(\mathbf{c}|n)\; p(\boldsymbol{\mu}|n)\; p(\mathbf{h}) \tag{B.4}$$

where n is the number of Voronoi nuclei, $p(n)$ is the prior on the number of Voronoi nuclei/cells, $p(\mathbf{c}|n)$ is the prior on Voronoi nuclei location, $p(\boldsymbol{\mu}|n)$ is the prior on cell log(resistivity), and $p(\mathbf{h})$ is the prior on noise hyperparameters.

The prior on the number of Voronoi cells $p(n)$ is a discrete Uniform distribution between a minimum (n^{min}) and a maximum (n^{max}) number of Voronoi nuclei, such that

$$p(n) = \begin{cases} \frac{1}{\Delta n} & \text{if } n \in \mathcal{N} \\ 0 & \text{otherwise} \end{cases} \tag{B.5}$$

where $\mathcal{N} = \left[n^{min}, n^{min}+1, ..., n^{max}-1, n^{max}\right]$ and $\Delta n = \left(n^{max} - n^{min} + 1\right)$.

In order to evaluate the prior on Voronoi cell locations $p(\mathbf{c}|n)$, we define a rectangular area bounded in x and z by $\left[x^{min}, x^{max}\right]$ and $\left[z^{min}, z^{max}\right]$ within which Voronoi nuclei may be located. For simplicity, let us assume that this rectangle can be discretised into a fictitious grid of N points at which Voronoi nuclei can be located (where $N = N_x \times N_z$). For n Voronoi nuclei there then exist $\frac{N!}{n!(N-n)!}$ ways in which the nuclei can be arranged, all having the same probability. Hence, the prior on Voronoi nuclei location is given by

$$p(\mathbf{c}|n) = \begin{cases} \left(\frac{N!}{n!\,(N-n)!}\right)^{-1} & \forall i \in [1,n],\, x_i \in \mathcal{X} \text{ and } z_i \in \mathcal{Z} \\ 0 & \text{otherwise} \end{cases} \tag{B.6}$$

where $\mathcal{X} = \left[x^{min}, x^{max}\right]$ and $\mathcal{Z} = \left[z^{min}, z^{max}\right]$. Alternatively, the prior on Voronoi cell locations may be set to a Dirichlet distribution as discussed by *Steininger et al.* [2013], which precludes the need for a fictitious grid to be defined.

The prior on cell resistivity is a continuous Uniform distribution bounded by a minimum (μ^{min}) and a maximum (μ^{max}) log(resistivity) value, such that for each cell i

$$p(\mu_i|n) = \begin{cases} \frac{1}{\Delta\mu} & \text{if } \mu_i \in \mathcal{M} \\ 0 & \text{otherwise} \end{cases} \tag{B.7}$$

where $\mathcal{M} = \left[\mu^{min}, \mu^{max}\right]$ and $\Delta\mu = \left(\mu^{max} - \mu^{min}\right)$. Since the resistivity of each cell is independent of that of any other cell, the prior over log(resistivity) for all cells is

$$p(\boldsymbol{\mu}|n) = c_\mu \prod_{i=1}^{n} p(\mu_i|n) \tag{B.8}$$

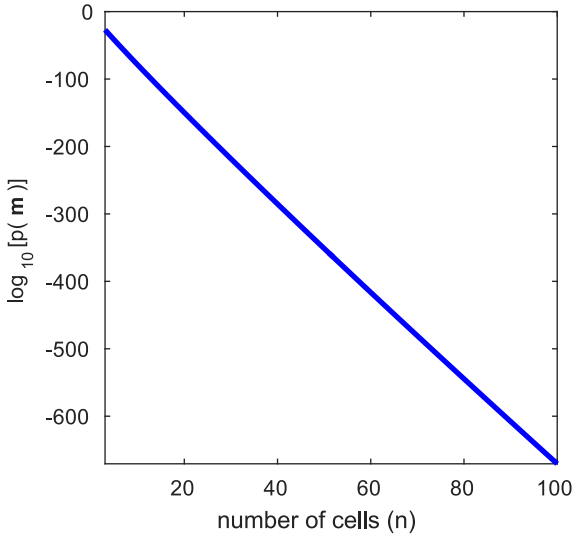

Figure B.1. Prior $p(\mathbf{m})$ as a function of number of cells n, calculated using equation B.11 and the prior parameters from the synthetic example in Section 3.1. Note that the y-axis uses a logarithmic scale.

where c_μ is a normalising constant, and $p(\boldsymbol{\mu}|n)$ is only greater than zero if the log(resistivity) of every cell falls within the interval $\left[\mu^{min}, \mu^{max}\right]$.

Similarly, the prior on the set of noise hyperparameters $\mathbf{h}$ is assigned assuming that all hyperparameters are mutually independent (in other words, without imposing any dependence between hyperparameters a priori). The prior on each hyperparameter h_j is described by a continuous Uniform distribution between a minimum (h_j^{min}) and a maximum (h_j^{max}) value such that

$$p(h_j) = \begin{cases} \frac{1}{\Delta h_j} & \text{if } h_j \in \mathcal{H}_j \\ 0 & \text{otherwise} \end{cases} \tag{B.9}$$

where $\mathcal{H}_j = \left[h_j^{min}, h_j^{max}\right]$ and $\Delta h_j = \left(h_j^{max} - h_j^{min}\right)$. Since each hyperparameter is independent of all the others, the prior over all hyperparameters is

$$p(\mathbf{h}) = c_h \prod_{j=1}^{J} p(h_j) \tag{B.10}$$

where c_h is a normalising constant and J is the total number of hyperparameters.

By combining equations B.5, B.6, B.8 and B.10 as in equation B.4, the full prior probability density function can be expressed as

$$p(\mathbf{m}) = \frac{c_m \; n! \; (N-n)!}{N! \; (\Delta\mu)^n \; \Delta n \left(\prod_{j=1}^{J} \Delta h_j\right)} \tag{B.11}$$

where $c_m = c_\mu \; c_h$, provided that all parameters fall within the boundaries of their respective priors. If one of the parameters falls outside of the range of its prior, the full prior in equation B.11 becomes zero. As an example, the prior calculated from equation B.11 using the prior parameters from the synthetic example in Section 3.1 is shown in Figure B.1.

B.3 Proposal distributions

At each step of the Markov chain, a perturbed model $\mathbf{m}'$ is drawn from a proposal distribution $q(\mathbf{m}'|\mathbf{m})$, which is only dependent on the present model $\mathbf{m}$ and which might take

the form

$$q(\mathbf{m}'|\mathbf{m}) \propto \exp\left\{-\frac{1}{2}\,(\mathbf{m}-\mathbf{m}')^{\mathrm{T}}\,\mathbf{C}^{-1}\,(\mathbf{m}-\mathbf{m}')\right\} \tag{B.12}$$

representing a Gaussian distribution with mean $\mathbf{m}$ and with a typically diagonal covariance matrix $\mathbf{C}$. In practical applications, in order to create a new model $\mathbf{m}'$ from the current model $\mathbf{m}$ the i^{th} component of $\mathbf{m}$ may be perturbed according to the proposal distribution as

$$\mathbf{m}' = \mathbf{m} + u\sigma_i\mathbf{e}_i \tag{B.13}$$

where u is a random deviate from a standard normal distribution (a Gaussian with mean of 0 and variance of 1), σ_i is the standard deviation of the proposal (step size), and $\mathbf{e}_i$ is a unit vector in the i^{th} direction. Overall, five types of perturbations can be performed on the model $\mathbf{m}$ used here:

- A *resistivity* step perturbs the resistivity of a randomly-selected cell. If the resistivity of cell i is to be perturbed, a new log(resistivity) value μ_i' for the cell can be obtained from

$$\mu_i' = \mu_i + u\sigma_r \tag{B.14}$$

  where μ_i is the present log(resistivity) of cell i, and σ_r is the step size of the proposal for a change in cell log(resistivity).
- A *move* step changes the position of a randomly-selected Voronoi nucleus. If the location of cell i is to be perturbed, a new location $\mathbf{c}_i'$ (given by coordinates x_i' and z_i') for the cell nucleus can be obtained from

$$\begin{aligned} x_i' &= x_i + u\sigma_c \\ z_i' &= z_i + u\sigma_c \end{aligned} \tag{B.15}$$

  where x_i and z_i are the current x and z coordinates of nucleus i, and σ_c is the step size of the proposal for a change in cell location.
- A *death* step removes a randomly-selected Voronoi cell nucleus from the model vector $\mathbf{m}$.
- A *birth* step adds a Voronoi cell nucleus to the current model. If a new cell is added at a random location $\mathbf{c}_{n+1}'$, the log(resistivity) of the new cell is obtained from

$$\mu_{n+1}' = \mu_i + u\sigma_{bd} \tag{B.16}$$

  where μ_i is the present log(resistivity) at location $\mathbf{c}_{n+1}'$, and σ_{bd} is the step size of the resistivity proposal in the case of birth and death steps.
- A *noise* step perturbs a randomly-selected data noise hyperparameter. If noise hyperparameter h_j is perturbed (while the resistivity structure of the model remains unchanged), a new hyperparameter h_j' can be obtained from

$$h_j' = h_j + u\sigma_{h_j} \tag{B.17}$$

  where h_j is the current value of hyperparameter j, and σ_{h_j} is the step size of the proposal for a change in h_j.

B.4 The acceptance parameter α

The use of $\alpha(\mathbf{m}'|\mathbf{m})$ as an acceptance parameter in step 6 of the TERT algorithm ensures that, for perturbation types of *fixed* dimensionality (i.e., changing resistivity and noise, and moving a Voronoi nucleus), all models that improve the data fit are accepted and those that do not are randomly accepted or rejected depending on their likelihood, while in the case of perturbation types involving a change in model dimension (i.e., birth and death steps) the acceptance of proposed models involves a balance between likelihood, prior and proposal ratios (as discussed in more detail in Section 5.4). *Green* [1995, 2003] showed that this in

turn ensures that the sample population follows the posterior distribution $p(\mathbf{m}|\mathbf{d}^{obs})$ as the number of iterations tends to infinity.

As can be seen in equation 5, the expression for the acceptance ratio $\alpha(\mathbf{m}'|\mathbf{m})$ involves the product of prior, likelihood and proposal ratios and the Jacobian of the transformation from $\mathbf{m}$ to $\mathbf{m}'$. A detailed derivation of all of these terms can be found in *Bodin and Sambridge* [2009] for the case of seismic traveltime tomography, and the derivation is almost identical for TERT. Since to the best of our knowledge this transdimensional inversion algorithm has not previously been used in electrical resistivity tomography, here we briefly introduce each term in equation 5.

The calculation of the prior ratio involves the evaluation of the prior for $\mathbf{m}$ and $\mathbf{m}'$ using equation B.11. In the case of perturbation types of *fixed* dimensionality, $p(\mathbf{m}) = p(\mathbf{m}')$, hence the prior ratio is unity provided that the proposed values fall within the support of their respective priors (the support is the set of values for which the probability is non-zero):

$$\left[\frac{p(\mathbf{m}')}{p(\mathbf{m})}\right]_{fixed} = \begin{cases} 1 & \text{if } \mathbf{m}' \in \mathcal{N}, \mathcal{M}, \mathcal{X}, \mathcal{Z}, \mathcal{H} \\ 0 & \text{otherwise} \end{cases} \tag{B.18}$$

For perturbation types which involve a jump in dimensionality, the prior ratio for a birth step is

$$\left[\frac{p(\mathbf{m}')}{p(\mathbf{m})}\right]_{birth} = \begin{cases} \frac{n+1}{(N-n)\,\Delta\mu} & \text{if } \mathbf{m}' \in \mathcal{N}, \mathcal{M}, \mathcal{X}, \mathcal{Z}, \mathcal{H} \\ 0 & \text{otherwise} \end{cases} \tag{B.19}$$

and for a death step is

$$\left[\frac{p(\mathbf{m}')}{p(\mathbf{m})}\right]_{death} = \begin{cases} \frac{(N-n+1)\,\Delta\mu}{n} & \text{if } \mathbf{m}' \in \mathcal{N}, \mathcal{M}, \mathcal{X}, \mathcal{Z}, \mathcal{H} \\ 0 & \text{otherwise} \end{cases} \tag{B.20}$$

For perturbations that change the resistivity structure of the model, the evaluation of the likelihood ratio involves the computation of the electrical potential Φ generated by each pair of current electrodes through the Voronoi tessellation of $\mathbf{m}$ and $\mathbf{m}'$, and the calculation of potential differences (and data uncertainties if necessary – equation 4) for all required combinations of current and potential electrodes. For noise perturbations it requires only the calculation of new data uncertainties. Once all potential differences and/or noise parameters have been calculated, the likelihood function may be evaluated using equation B.3, giving

$$\frac{p(\mathbf{d}^{obs}|\mathbf{m}')}{p(\mathbf{d}^{obs}|\mathbf{m})} = \left(\prod_{k=1}^{K} \frac{\sigma_k}{\sigma'_k}\right) \exp\left\{-\frac{\psi(\mathbf{m}') - \psi(\mathbf{m})}{2}\right\} \tag{B.21}$$

where σ_k and σ'_k are the current and proposed uncertainties associated with the k^{th} datum, respectively.

The proposal probability $q(\mathbf{m}'|\mathbf{m})$ expresses the probability to move from $\mathbf{m}$ to $\mathbf{m}'$, while $q(\mathbf{m}|\mathbf{m}')$ expresses the probability for the reverse move, from $\mathbf{m}'$ to $\mathbf{m}$. In the case of perturbation types which do not involve a change in dimension, $q(\mathbf{m}'|\mathbf{m})$ and $q(\mathbf{m}|\mathbf{m}')$ are symmetrical distributions, hence their ratio is unity:

$$\left[\frac{q(\mathbf{m}|\mathbf{m}')}{q(\mathbf{m}'|\mathbf{m})}\right]_{fixed} = 1 \tag{B.22}$$

For perturbation types which involve a jump in dimension, the proposal distributions $q(\mathbf{m}'|\mathbf{m})$ and $q(\mathbf{m}|\mathbf{m}')$ are not symmetric and we obtain different proposal ratios depending on the type of perturbation. For a birth step which creates a new cell at location $\mathbf{c}'_{n+1}$ the ratio is

$$\left[\frac{q(\mathbf{m}|\mathbf{m}')}{q(\mathbf{m}'|\mathbf{m})}\right]_{birth} = \frac{\sqrt{2\pi}\,(N-n)}{n+1}\,\sigma_{bd}\,\exp\left\{\frac{(\mu'_{n+1} - \mu_i)^2}{2\sigma_{bd}^2}\right\} \tag{B.23}$$

where μ'_{n+1} is the log(resistivity) of the added cell, μ_i is the present log(resistivity) at location $\mathbf{c}'_{n+1}$, and σ_{bd} is defined in equation B.16. For a death step which involves the deletion of cell i the proposal ratio is

$$\left[\frac{q(\mathbf{m}|\mathbf{m}')}{q(\mathbf{m}'|\mathbf{m})}\right]_{death} = \frac{n}{\sigma_{bd}\sqrt{2\pi}\,(N-n+1)} \exp\left\{-\frac{(\mu'_j-\mu_i)^2}{2\sigma_{bd}^2}\right\} \tag{B.24}$$

where μ'_j is the log(resistivity) at $\mathbf{c}_i$ in the new tessellation (i.e., after the deletion of cell i).

The Jacobian term $|\mathbf{J}|$ accounts for scale changes occurring in the case of transdimensional perturbations by normalising the difference in volume of the two model spaces of different dimension [*Green*, 2003]. Besides being equal to one in the case of model perturbations which do not involve a change in dimension, *Bodin and Sambridge* [2009] show that $|\mathbf{J}|$ is unity even for birth and death steps, hence can be ignored.

By substituting the expressions for the Jacobian and for the prior, likelihood and proposal ratio into equation 5, an expression for $\alpha(\mathbf{m}'|\mathbf{m})$ can be obtained for each type of model perturbation. For model perturbations which do not involve a change in dimension, the product of ratios in equation 5 becomes simply the ratio of likelihoods in the proposed and current model since the prior and proposal ratios are both unity:

$$\alpha(\mathbf{m}'|\mathbf{m})_{fixed} = \begin{cases} \min\left[1, \left(\prod_{k=1}^{K}\frac{\sigma_k}{\sigma'_k}\right)\exp\left\{-\frac{\psi(\mathbf{m}')-\psi(\mathbf{m})}{2}\right\}\right] & \text{if } \mathbf{m}' \in \mathcal{N},\mathcal{M},\mathcal{X},\mathcal{Z},\mathcal{H} \\ 0 & \text{otherwise} \end{cases} \tag{B.25}$$

For model perturbations involving a change in dimension, for a birth step

$$\alpha(\mathbf{m}'|\mathbf{m})_{birth} = \begin{cases} \min\left[1, \frac{\sigma_{bd}\sqrt{2\pi}}{\Delta\mu}\left(\prod_{k=1}^{K}\frac{\sigma_k}{\sigma'_k}\right)\exp\left\{\frac{(\mu'_{n+1}-\mu_i)^2}{2\sigma_{bd}^2}-\frac{\psi(\mathbf{m}')-\psi(\mathbf{m})}{2}\right\}\right] & \text{if } \mathbf{m}' \in \mathcal{N},\mathcal{M},\mathcal{X},\mathcal{Z},\mathcal{H} \\ 0 & \text{otherwise} \end{cases} \tag{B.26}$$

and for a death step

$$\alpha(\mathbf{m}'|\mathbf{m})_{death} = \begin{cases} \min\left[1, \frac{\Delta\mu}{\sigma_{bd}\sqrt{2\pi}}\left(\prod_{k=1}^{K}\frac{\sigma_k}{\sigma'_k}\right)\exp\left\{-\frac{(\mu'_j-\mu_i)^2}{2\sigma_{bd}^2}-\frac{\psi(\mathbf{m}')-\psi(\mathbf{m})}{2}\right\}\right] & \text{if } \mathbf{m}' \in \mathcal{N},\mathcal{M},\mathcal{X},\mathcal{Z},\mathcal{H} \\ 0 & \text{otherwise} \end{cases} \tag{B.27}$$

Note that, since equations B.25–B.27 do not contain variable N (previously defined in equation B.6), the priors over x and z are here given over the continuous ranges $\mathcal{X} = \left[x^{min}, x^{max}\right]$ and $\mathcal{Z} = \left[z^{min}, z^{max}\right]$.

B.5 Statistical solutions

At the end of the inversion, maps showing different statistical properties of the subsurface resistivity field may be obtained from the ensemble by calculating a number of statistical moments through a regular grid of discrete points $[\bar{x}_i \;\; \bar{z}_i]$ over the M samples in the ensemble. These statistical properties may include (but are not limited to) the following measures:

- the *arithmetic mean* (i.e., the average or first statistical moment), given by

$$\bar{\mu} = \frac{1}{M}\sum_{m=1}^{M}\mu_m \tag{B.28}$$

  This statistic is ideal in purely Gaussian PDFs, but may be heavily affected by outliers or by the tails of the distribution when the posterior is not Gaussian.
- the *harmonic mean*, given by

$$\mathrm{HM}(\mu) = \frac{1}{\frac{1}{M}\sum_{m=1}^{M}\frac{1}{\mu_m}} \tag{B.29}$$

Since the harmonic mean involves taking the inverse of each value, this statistic is more sensitive to low resistivities within the ensemble than is the arithmetic mean.

- the *root-mean-square*, given by

$$\mathrm{RMS}(\mu) = \sqrt{\frac{1}{M}\sum_{m=1}^{M}\mu_m^2} \tag{B.30}$$

Since the root-mean-square involves squaring each value, this statistic is more sensitive to high resistivities within the ensemble than the arithmetic mean.

- the *median*, which can be defined as the parameter value that separates the lower half from the upper half of probabilities in the PDF. It is a robust statistic which is less affected by extremely large or small values than the arithmetic mean.
- the *mode*, or *maximum-a-posteriori* value, which can be defined as the parameter value appearing most often in the ensemble, and hence which has the largest value of the posterior PDF. Compared to the previous statistics, it tends to preserve the discrete character of the underlying Voronoi cells in the ensemble, hence maps of this statistical moment are normally characterised by sharp discontinuities between structures of different resistivity.
- the *standard deviation* (i.e., the square root of the second statistical moment), given by

$$\sigma_\mu = \sqrt{\frac{1}{M}\sum_{m=1}^{M}(\mu_m - \bar{\mu})^2} \tag{B.31}$$

This statistic is particularly useful within a stochastic inversion scheme as it provides a direct measure of the uncertainty in the solution.

- *entropy*, given by

$$\mathrm{Entropy}(\mu) = \sum_{j=1}^{J}\left[-p_j \ \log_2(p_j)\right] \tag{B.32}$$

where J is the number of bins in a histogram representing the posterior PDF on log(resistivity) at location $[\bar{x}_i \ \ \bar{z}_i]$ (see Figure 6), and p_j is the probability of log(resistivity) μ_j in the posterior PDF. Entropy can be described as a measure of disorder (lack of information), hence it is high at locations where the PDF resembles the Uniform prior (e.g., Figure 6(a)), and low where the posterior PDF is represented by sharp and well-defined peaks (e.g., Figure 6(e)).

- *skewness* (i.e., the third statistical moment), given by

$$\mathrm{Skewness}(\mu) = \frac{1}{\sigma_\mu^3}\left(\frac{1}{M}\sum_{m=1}^{M}\mu_m^3 - 3\bar{\mu}\frac{1}{M}\sum_{m=1}^{M}\mu_m^2 + 2\bar{\mu}^3\right) \tag{B.33}$$

This statistic provides information on the asymmetry of the PDF, with negatively-skewed distributions having a longer tail to the left and positively-skewed distributions having a longer tail to the right. Since a Gaussian distribution is symmetric around its arithmetic mean, purely Gaussian PDFs have zero skewness.

- *excess kurtosis* (i.e., the fourth statistical moment), given by

$$\mathrm{ExKurtosis}(\mu) = \frac{1}{\sigma_\mu^4}\left(\frac{1}{M}\sum_{m=1}^{M}\mu_m^4 - 4\bar{\mu}\frac{1}{M}\sum_{m=1}^{M}\mu_m^3 + 6\bar{\mu}^2\frac{1}{M}\sum_{m=1}^{M}\mu_m^2 - 3\bar{\mu}^4\right) - 3 \tag{B.34}$$

This statistic can be used to obtain information on the 'peakedness' of the PDF, with negative excess kurtosis indicating broader and flatter distributions (such as a Uniform distribution), and positive excess kurtosis indicating more 'pointy' distributions with flatter tails and narrower peaks (such as a Laplacian distribution). In addition, negative kurtosis can also indicate bimodal distributions which may be observed at sharp discontinuities (e.g., Figure 8).

Acknowledgments

We thank Thomas Bodin, Malcolm Sambridge, Florian Wellmann and Kees Weemstra for many enlightening discussions on transdimensional methods and uncertainty estimation, and André Revil, Andrew Binley, Anandaroop Ray and two anonymous reviewers for their constructive comments and suggestions which greatly improved this paper. We also thank Tina Wunderlich for providing the dataset that created our observational data example in the Supporting Information, Nathan Rowan for his contribution to the Glebe Field surveys, and AOC Archaeology for assistance with the interpretation of the results shown in Section 4.1. Finally, we thank the FracRisk consortium (Grant Agreement number: 636811 – FracRisk – H2020-LCE-2014-2015/H2020-LCE-2014-1) for funding this research and granting us permission to publish. Our inversion code and the data used in the examples presented will be made publicly available upon publication.

References

Andersen, K. E., S. P. Brooks, and M. B. Hansen (2003), Bayesian inversion of geoelectrical resistivity data, *Journal of the Royal Statistical Society: Series B (Statistical Methodology)*, *65*(3), 619–642, doi:10.1111/1467-9868.00406.

Aster, R. C., B. Borchers, and C. H. Thurber (2013), *Parameter Estimation and Inverse Problems*, 2 ed., Academic Press.

Bayes, M., and M. Price (1763), An Essay towards Solving a Problem in the Doctrine of Chances. By the Late Rev. Mr. Bayes, F. R. S. Communicated by Mr. Price, in a Letter to John Canton, A. M. F. R. S., *Philosophical Transactions*, *53*, 370–418, doi:10.1098/rstl.1763.0053.

Binley, A. (2013a), *R3t version 1.8 (March 2013)*, University of Lancaster.

Binley, A. (2013b), *R2 version 2.7a (February 2013)*, University of Lancaster.

Binley, A., and A. Kemna (2005), DC Resistivity and Induced Polarization Methods, in *Hydrogeophysics*, edited by Y. Rubin and S. S. Hubbard, pp. 129–156, Springer, Dordrecht, Netherlands, doi:10/fbvn2m.

Binley, A. M., A. Ramirez, and W. Daily (1995), Regularised Image Reconstruction of Noisy Electrical resistance Tomography Data, in *Proceedings of the 4th Workshop of the European Concerted Action on Process Tomography*, edited by M. S. Beck, pp. 401–410.

Blackwell, A. (2008), Geophysical Survey at Butchers and Glebe Fields, Aberlady.

Bodin, T., and M. Sambridge (2009), Seismic tomography with the reversible jump algorithm, *Geophysical Journal International*, *178*(3), 1411–1436, doi:10.1111/j.1365-246X.2009.04226.x.

Bodin, T., M. Sambridge, and K. Gallagher (2009), A self-parametrizing partition model approach to tomographic inverse problems, *Inverse Problems*, *25*(5), 055,009.

Bodin, T., M. Sambridge, H. Tkalv cić, P. Arroucau, K. Gallagher, and N. Rawlinson (2012a), Transdimensional inversion of receiver functions and surface wave dispersion, *Journal of Geophysical Research: Solid Earth*, *117*(B2), doi:10.1029/2011JB008560.

Bodin, T., M. Sambridge, N. Rawlinson, and P. Arroucau (2012b), Transdimensional tomography with unknown data noise, *Geophysical Journal International*, *189*(3), 1536–1556, doi:10.1111/j.1365-246X.2012.05414.x.

Bottero, A., A. Gesret, T. Romary, M. Noble, and C. Maisons (2016), Stochastic seismic tomography by interacting Markov chains, *Geophysical Journal International*, *207*(1), 374–392, doi:10.1093/gji/ggw272.

Brooks, B. A., and L. Neil Frazer (2005), Importance reweighting reduces dependence on temperature in Gibbs samplers: an application to the coseismic geodetic inverse problem, *Geophysical Journal International*, *161*(1), 12–20, doi:10.1111/j.1365-246X.2005.02573.x.

Brooks, S. P., and A. Gelman (1998), General Methods for Monitoring Convergence of Iterative Simulations, *Journal of Computational and Graphical Statistics*, *7*(4), 434–455.

Curtis, A. (1999a), Optimal design of focused experiments and surveys, *Geophysical Journal International*, *139*(1), 205–215, doi:10.1046/j.1365-246X.1999.00947.x.

Curtis, A. (1999b), Optimal experiment design: cross-borehole tomographic examples, *Geophysical Journal International*, *136*(3), 637–650, doi:10.1046/j.1365-246x.1999.00749.x.

Curtis, A., and A. Lomax (2001), Prior information, sampling distributions, and the curse of dimensionality, *Geophysics*, *66*(2), 372–378, doi:10.1190/1.1444928.

Curtis, A., and R. Snieder (2002), Probing the Earth's interior with seismic tomography, in *International Handbook of Earthquake and Engineering Seismology*, *International Geophysics*, vol. 81, Part A, edited by William and C. Kisslinger, chap. 52, Academic Press, doi:http://dx.doi.org/10.1016/S0074-6142(02)80259-5.

Dettmer, J., S. E. Dosso, and C. W. Holland (2010), Trans-dimensional geoacoustic inversion, *The Journal of the Acoustical Society of America*, *128*(6), 3393–3405, doi:http://dx.doi.org/10.1121/1.3500674.

Dettmer, J., R. Benavente, P. R. Cummins, and M. Sambridge (2014), Trans-dimensional finite-fault inversion, *Geophysical Journal International*, *199*(2), 735–751, doi:10.1093/gji/ggu280.

Dettmer, J., S. E. Dosso, T. Bodin, J. Stipčević, and P. R. Cummins (2015), Direct-seismogram inversion for receiver-side structure with uncertain sourceâĂŞtime functions, *Geophysical Journal International*, *203*(2), 1373–1387, doi:10.1093/gji/ggv375.

Dey, A., and H. F. Morrison (1979a), Resistivity Modelling for Arbitrarily Shaped Two-Dimensional Structures, *Geophysical Prospecting*, *27*(1), 106–136, doi:10.1111/j.1365-2478.1979.tb00961.x.

Dey, A., and H. F. Morrison (1979b), Resistivity modeling for arbitrarily shaped three-dimensional structures, *Geophysics*, *44*(4), 753–780, doi:10.1190/1.1440975.

Dosso, S. E., C. W. Holland, and M. Sambridge (2012), Parallel tempering for strongly nonlinear geoacoustic inversion, *The Journal of the Acoustical Society of America*, *132*(5), 3030–3040, doi:http://dx.doi.org/10.1121/1.4757639.

Dosso, S. E., J. Dettmer, G. Steininger, and C. W. Holland (2014), Efficient trans-dimensional Bayesian inversion for geoacoustic profile estimation, *The Journal of the Acoustical Society of America*, *136*(4), 2085, doi:10.1121/1.4899489.

Earl, D. J., and M. W. Deem (2005), Parallel tempering: Theory, applications, and new perspectives, *Physical Chemistry Chemical Physics*, *7*, 3910–3916, doi:10.1039/B509983H.

Edwards, L. S. (1977), A Modified Pseudosection for Resistivity and IP, *Geophysics*, *42*(5), 1020–1036, doi:10.1190/1.1440762.

Galetti, E., A. Curtis, G. A. Meles, and B. Baptie (2015), Uncertainty loops in travel-time tomography from nonlinear wave physics, *Physical Review Letters*, *114*(14), 148,501.

Gallagher, K., T. Bodin, M. Sambridge, D. Weiss, M. Kylander, and D. Large (2011), Inference of abrupt changes in noisy geochemical records using transdimensional changepoint models, *Earth and Planetary Science Letters*, *311*, 182–194, doi:http://dx.doi.org/10.1016/j.epsl.2011.09.015.

Gelman, A., and D. B. Rubin (1992), Inference from Iterative Simulation Using Multiple Sequences, *Statistical Science*, *7*(4), 457–472.

Gelman, A., G. Roberts, and W. Gilks (1996), Efficient Metropolis Jumping Rules, *Bayesian Statistics*, *5*(599–608), 42.

Green, P. J. (1995), Reversible jump Markov chain Monte Carlo computation and Bayesian model determination, *Biometrika*, *82*(4), 711–732, doi:10.1093/biomet/82.4.711.

Green, P. J. (2003), Trans-dimensional Markov chain Monte Carlo, in *Highly Structured Stochastic Systems*, *Oxford Statistical Science Series*, vol. 27, edited by P. J. Green, N. Lid Hjort, and S. Richardson, chap. 6, pp. 179–198, Oxford University Press.

Green, P. J., and A. Mira (2001), Delayed Rejection in Reversible Jump Metropolis-Hastings, *Biometrika*, *88*(4), 1035–1053.

Hastings, W. K. (1970), Monte Carlo sampling methods using Markov chains and their applications, *Biometrika*, *57*(1), 97–109, doi:10.1093/biomet/57.1.97.

Hawkins, R., and M. Sambridge (2015), Geophysical imaging using trans-dimensional trees, *Geophysical Journal International*, *203*(2), 972–1000, doi:10.1093/gji/ggv326.

Hawkins, R., M. Sambridge, and R. C. Brodie (2017), Trans-dimensional Bayesian inversion of airborne electromagnetic data for 2D conductivity profiles, *Exploration Geophysics*, doi:10.1071/EG16139.

Irving, J., and K. Singha (2010), Stochastic inversion of tracer test and electrical geophysical data to estimate hydraulic conductivities, *Water Resources Research*, *46*(11), doi:10.1029/2009WR008340.

JafarGandomi, A., and A. Binley (2013), A Bayesian trans-dimensional approach for the fusion of multiple geophysical datasets, *Journal of Applied Geophysics*, *96*, 38–54, doi:https://doi.org/10.1016/j.jappgeo.2013.06.004.

Jardani, A., A. Revil, and J. P. Dupont (2013), Stochastic joint inversion of hydrogeophysical data for salt tracer test monitoring and hydraulic conductivity imaging, *Advances in Water Resources*, *52*, 62–77, doi:https://doi.org/10.1016/j.advwatres.2012.08.005.

Kaipio, J. P., V. Kolehmainen, E. Somersalo, and M. Vauhkonen (2000), Statistical inversion and Monte Carlo sampling methods in electrical impedance tomography, *Inverse Problems*, *16*(5), 1487.

Koefoed, O. (1979), *Geosounding Principles 1: Resistivity Sounding Measurements*, Methods in Geochemistry and Geophysics, Elsevier, Amsterdam.

Li, Y., and K. Spitzer (2002), Three-dimensional DC resistivity forward modelling using finite elements in comparison with finite-difference solutions, *Geophysical Journal International*, *151*(3), 924–934, doi:10.1046/j.1365-246X.2002.01819.x.

Linde, N., A. Binley, A. Tryggvason, L. B. Pedersen, and A. Revil (2006), Improved hydrogeophysical characterization using joint inversion of cross-hole electrical resistance and ground-penetrating radar traveltime data, *Water Resources Research*, *42*(12), doi:10.1029/2006WR005131.

Link, W. A., and M. J. Eaton (2011), On thinning of chains in MCMC, *Methods in Ecology and Evolution*, *3*(1), 112–115, doi:10.1111/j.2041-210X.2011.00131.x.

Loke, M. H. (1994), The inversion of two-dimensional resistivity data, Ph.D. thesis, University of Birmingham.

Lowry, T., M. B. Allen, and P. N. Shive (1989), Singularity removal; a refinement of resistivity modeling techniques, *Geophysics*, *54*(6), 766–774, doi:10.1190/1.1442704.

MacKay, D. J. C. (2003), *Information Theory, Inference and Learning Algorithms*, 640 pp., Cambridge University Press, University of Cambridge, doi:10.1007/b98673.

Malinverno, A. (2002), Parsimonious Bayesian Markov chain Monte Carlo inversion in a nonlinear geophysical problem, *Geophysical Journal International*, *151*(3), 675–688, doi:10.1046/j.1365-246X.2002.01847.x.

Maurer, H., D. E. Boerner, and A. Curtis (2000), Design strategies for electromagnetic geophysical surveys, *Inverse Problems*, *16*(5), 1097.

Metropolis, N., A. W. Rosenbluth, M. N. Rosenbluth, A. H. Teller, and E. Teller (1953), Equation of State Calculations by Fast Computing Machines, *The Journal of Chemical Physics*, *21*(6), 1087–1092, doi:http://dx.doi.org/10.1063/1.1699114.

Minsley, B. J. (2011), A trans-dimensional Bayesian Markov chain Monte Carlo algorithm for model assessment using frequency-domain electromagnetic data, *Geophysical Journal International*, *187*(1), 252–272, doi:10.1111/j.1365-246X.2011.05165.x.

Mosegaard, K., and A. Tarantola (1995), Monte Carlo sampling of solutions to inverse problems, *Journal of Geophysical Research: Solid Earth*, *100*(B7), 12,431–12,447, doi:10.1029/94JB03097.

Neighbour, T., W. Shaw, and E. Cavanagh (1995), Kilspindie Castle: geophysical survey, a preliminary report, *Tech. rep.*

Neighbour, T., B. Tulloch, and C. Davis (1998), Kilspindie Castle: geophysical survey, a preliminary report, *Tech. rep.*

Parker, R. L. (1994), *Geophysical Inverse Theory*, Princeton University Press.

Pidlisecky, A., and R. Knight (2008), FW2_5D: A MATLAB 2.5-D electrical resistivity modeling code, *Computers & Geosciences*, *34*(12), 1645–1654, doi:http://dx.doi.org/10.1016/j.cageo.2008.04.001.

Pridmore, D. F., G. W. Hohmann, S. H. Ward, and W. R. Sill (1981), An investigation of finite-element modeling for electrical and electromagnetic data in three dimensions, *Geophysics*, *46*(7), 1009–1024, doi:10.1190/1.1441239.

Ramirez, A. L., J. J. Nitao, W. G. Hanley, R. Aines, R. E. Glaser, S. K. Sengupta, K. M. Dyer, T. L. Hickling, and W. D. Daily (2005), Stochastic inversion of electrical resistivity changes using a Markov Chain Monte Carlo approach, *Journal of Geophysical Research: Solid Earth*, *110*(B2), doi:10.1029/2004JB003449, b02101.

Ray, A., D. L. Alumbaugh, G. M. Hoversten, and K. Key (2013), Robust and accelerated Bayesian inversion of marine controlled-source electromagnetic data using parallel tempering, *Geophysics*, *78*(6), E271–E280, doi:10.1190/geo2013-0128.1.

Ray, A., K. Key, T. Bodin, D. Myer, and S. Constable (2014), Bayesian inversion of marine CSEM data from the Scarborough gas field using a transdimensional 2-D parametrization, *Geophysical Journal International*, *199*(3), 1847–1860, doi:10.1093/gji/ggu370.

Ray, A., A. Sekar, G. M. Hoversten, and U. Albertin (2016), Frequency domain full waveform elastic inversion of marine seismic data from the Alba field using a Bayesian transdimensional algorithm, *Geophysical Journal International*, doi:10.1093/gji/ggw061.

Ray, A., S. Kaplan, J. Washbourne, and U. Albertin (2018), Low frequency full waveform seismic inversion within a tree based Bayesian framework, *Geophysical Journal International*, *212*(1), 522–542, doi:10.1093/gji/ggx428.

Rosas-Carbajal, M., N. Linde, T. Kalscheuer, and J. A. Vrugt (2014), Two-dimensional probabilistic inversion of plane-wave electromagnetic data: methodology, model constraints and joint inversion with electrical resistivity data, *Geophysical Journal International*, *196*(3), 1508–1524, doi:10.1093/gji/ggt482.

Roy, C., and B. A. Romanowicz (2017), On the Implications of A Priori Constraints in Transdimensional Bayesian Inversion for Continental Lithospheric Layering, *Journal of Geophysical Research: Solid Earth*, *122*(12), doi:10.1002/2017JB014968.

Rücker, C., T. Günther, and K. Spitzer (2006), Three-dimensional modelling and inversion of dc resistivity data incorporating topography - I. Modelling, *Geophysical Journal International*, *166*(2), 495–505, doi:10.1111/j.1365-246X.2006.03010.x.

Sambridge, M. (2014), A Parallel Tempering algorithm for probabilistic sampling and multimodal optimization, *Geophysical Journal International*, *196*(1), 357–374, doi:10.1093/gji/ggt342.

Sambridge, M., J. Braun, and H. McQueen (1995), Geophysical parametrization and interpolation of irregular data using natural neighbours, *Geophysical Journal International*, *122*(3), 837–857, doi:10.1111/j.1365-246X.1995.tb06841.x.

Scales, J. A., and R. Snieder (1997), To Bayes or not to Bayes?, *GEOPHYSICS*, *62*(4), 1045–1046, doi:10.1190/1.6241045.1.

Sherlock, C., and G. Roberts (2009), Optimal scaling of the random walk Metropolis on elliptically symmetric unimodal targets, *Bernoulli*, *15*(3), 774–798, doi:10.3150/08-BEJ176.

Simmons, N. A., S. C. Myers, G. Johannesson, and E. Matzel (2012), LLNL-G3Dv3: Global P wave tomography model for improved regional and teleseismic travel time prediction, *Journal of Geophysical Research: Solid Earth*, *117*(B10), doi:10.1029/2012JB009525.

Steininger, G., J. Dettmer, S. E. Dosso, and C. W. Holland (2013), Trans-dimensional joint inversion of seabed scattering and reflection data, *The Journal of the Acoustical Society of America*, *133*(3), 1347–1357, doi:10.1121/1.4789930.

Swendsen, R. H., and J.-S. Wang (1987), Nonuniversal critical dynamics in Monte Carlo simulations, *Phys. Rev. Lett.*, *58*, 86–88, doi:10.1103/PhysRevLett.58.86.

Tarantola, A. (2005), *Inverse Problem Theory and Methods for Model Parameter Estimation*, SIAM, doi:10.1137/1.9780898717921.

Telford, W. M., L. P. Geldart, and R. E. Sheriff (1991), *Applied Geophysics*, 2 ed., Cambridge University Press.

Tierney, L., and A. Mira (1999), Some adaptive Monte Carlo methods for Bayesian inference, *Statistics in Medicine*, *18*(17-18), 2507–2515, doi:10/br5gn5.

Tso, C.-H. M., O. Kuras, P. B. Wilkinson, S. Uhlemann, J. E. Chambers, P. I. Meldrum, J. Graham, E. F. Sherlock, and A. Binley (2017), Improved characterisation and modelling of measurement errors in electrical resistivity tomography (ERT) surveys, *Journal of Applied Geophysics*, *146*, 103–119, doi:https://doi.org/10.1016/j.jappgeo.2017.09.009.

Valentová, L., F. Gallovič, and P. Maierová (2017), Three-dimensional S-wave velocity model of the Bohemian Massif from Bayesian ambient noise tomography, *Tectonophysics*, *717*, 484–498, doi:https://doi.org/10.1016/j.tecto.2017.08.033.

Wilken, D., T. Wunderlich, H. Stümpel, W. Rabbel, R. Pav steka, E. Erkul, J. Papv co, R. Putiv ska, M. Krajv nák, and D. Kuv snirák (2015), Case history: integrated geophysical survey at Katarínka Monastery (Slovakia), *Near Surface Geophysics*, *13*(6), 585–599, doi:10.3997/1873-0604.2015027.

Young, M., N. Rawlinson, and T. Bodin (2013), Transdimensional inversion of ambient seismic noise for 3D shear velocity structure of the Tasmanian crust, *Geophysics*, *78*(3), WB49–WB62, doi:10.1190/geo2012-0356.1.

Supporting Information for "Transdimensional Electrical Resistivity Tomography"

E. Galetti[1] and A. Curtis[1]

1. Observational data experiments: Slovakia dataset

In this experiment, we inverted an observational dataset (donated courtesy of Tina Wunderlich at Kiel University) recorded at an archaeological site in the western Small Carpathians (Slovakia). A detailed investigation involving multiple geophysical techniques was carried out by *Wilken et al.* [2015] at this site with the purpose of imaging the ruins of a number of chapels belonging to the abandoned Franciscan monastery of Katarınka. *Wilken et al.* [2015] found that the combined interpretation of results from different methods (magnetics, ground penetrating radar and ERT) was particularly beneficial in that each technique complemented the others. Given that the same anomalies were imaged using

Corresponding author: E. Galetti, University of Edinburgh, School of GeoSciences, James Hutton Road, Edinburgh EH9 3FE, United Kingdom. (erica.galetti@ed.ac.uk)

[1]University of Edinburgh, School of GeoSciences, James Hutton Road, Edinburgh EH9 3FE, United Kingdom

multiple techniques, this dataset provides an ideal setting to test our inversion method on observational data.

We inverted a dataset recorded using a Wenner-alpha configuration and 51 electrodes with spacing 0.5 m (gray rectangles in Figures S1–S3), giving 408 measured potential differences in total. We assumed data noise to be unknown, hence also inverted for parameters a and b in equation 3 in the main text. A simplified model showing the interpretation of the profile by *Wilken et al.* [2015] is shown in Figure S1.

We assumed Uniform priors on the number of Voronoi cells as $[5, 6, ..., 200]$, on $\mu = \log(\rho)$ as $[0.5, 4.5]$, on the x and z coordinates of model boundaries as $[-2, 27]$ and $[0, 10]$, respectively, and on noise parameters a as $[0.0001, 0.2001]$ and b as $[0.1, 1.1]$, respectively. We ran 32 tempered Markov chains (of which 16 were at the target temperature $T_0 = 1$) in parallel for 1×10^6 iterations allowing two randomly-chosen chains to swap models at each iteration according to equation 7 in the main text. Every 100^{th} sample at the target temperature after a burn-in period of 2.5×10^5 iterations was considered as a representative model from the posterior PDF, giving an ensemble of 120×10^3 valid samples.

The results from the inversion using the TERT algorithm are shown in Figure S2. In this case, since the prior on log(resistivity) does not cross 0, we also include the harmonic mean among the statistical maps produced with TERT. Figure S3 shows the inversion results obtained using the linearised code *R2*, where data noise was assumed to be proportional to the measured resistances according to equation 3 in the main text, and a and b were obtained from the posterior calculated with TERT (Figure S4).

In all cases (a)–(e), a high resistivity anomaly is imaged near $[12, 2]$ m, together with a thin high-resistivity layer near the surface to its left. The central high-resistivity anomaly

corresponds to an anomaly which is also imaged with ground penetrating radar (see *Wilken et al.* [2015] for details), and was originally interpreted as a pot-shaped structure of high resistivity embedded in soil by *Wilken et al.* [2015] (Figure S1). The resistivity of the background medium is resolved differently by different statistical moments: as expected, the harmonic mean map is more sensitive to low resistivities in the ensemble and the root-mean-square map is more sensitive to high resistivity values, while both the arithmetic mean and the median seem to fall somewhere in between.

In terms of uncertainty, the standard deviation and entropy maps show that resolution is limited below 2 m depth. As expected, the density of Voronoi nuclei within the ensemble peaks near the surface, specifically near the thin, high-resistivity layer to the left of the central anomaly. This is intuitively correct since a large number of small Voronoi cells are required to describe smaller-scale structures.

Since we considered data noise as an unknown in the inversion, the posterior on noise hyperparameters a and b are shown in Figure S4. While parameter b peaks at 0.1 (i.e., the lower prior boundary, suggesting that the prior should have probably been extended below 0.1), parameter a peaks around 0.04, suggesting that the level of noise in this dataset is $\sim 4\%$.

The thin high-resistivity layer and the central anomaly are also resolved by the iterated-linearised inversion with code *R2*. However, while sensitivity can be calculated (Figure S3(b)), a map of uncertainty is not produced with this code so it is not possible to associate a measure of the accuracy of the reconstructed structure in Figure S3(a). In addition, some of the maps retrieved through TERT (i.e., Figure S2(a)–(e)) seem to indicate the presence of a high-resistivity structure near $[20, 3]$ m which is not resolved at

all by linearised inversion. Although it is located in an area of high standard deviation and entropy (Figure S2(g)–(h)), the synthetic examples in Section 3 of the main text showed that mean structure may be correctly retrieved with TERT even in regions of high uncertainty, hence it is possible that this anomaly represents a high-resistivity body embedded in soil.

References

Binley, A. (2013), *R2 version 2.7a (February 2013)*, University of Lancaster.

Wilken, D., T. Wunderlich, H. Stümpel, W. Rabbel, R. Pav steka, E. Erkul, J. Papv co, R. Putiv ska, M. Krajv nák, and D. Kuv snirák (2015), Case history: integrated geophysical survey at Katarínka Monastery (Slovakia), *Near Surface Geophysics*, *13*(6), 585–599, doi:10.3997/1873-0604.2015027.

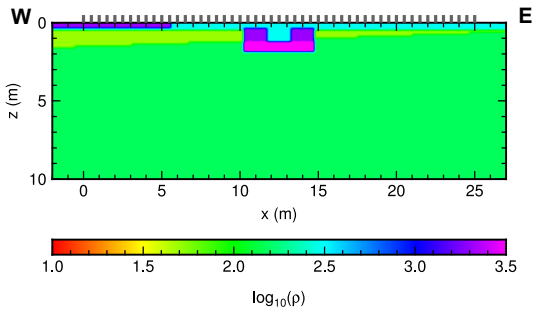

Figure S1. Simplified model showing *Wilken et al.* [2015]'s interpretation of the profile that we imaged using the TERT algorithm. A u-shaped high-resistivity anomaly embedded in low-resistivity material (i.e., soil) is visible near the centre of the profile, together with a thin, high-resistivity layer near the surface to the west of the anomaly. Re-plotted after Figure 11(c) in *Wilken et al.* [2015]. The grey ticks at $z = 0$ m denote electrode locations used in our inversion.

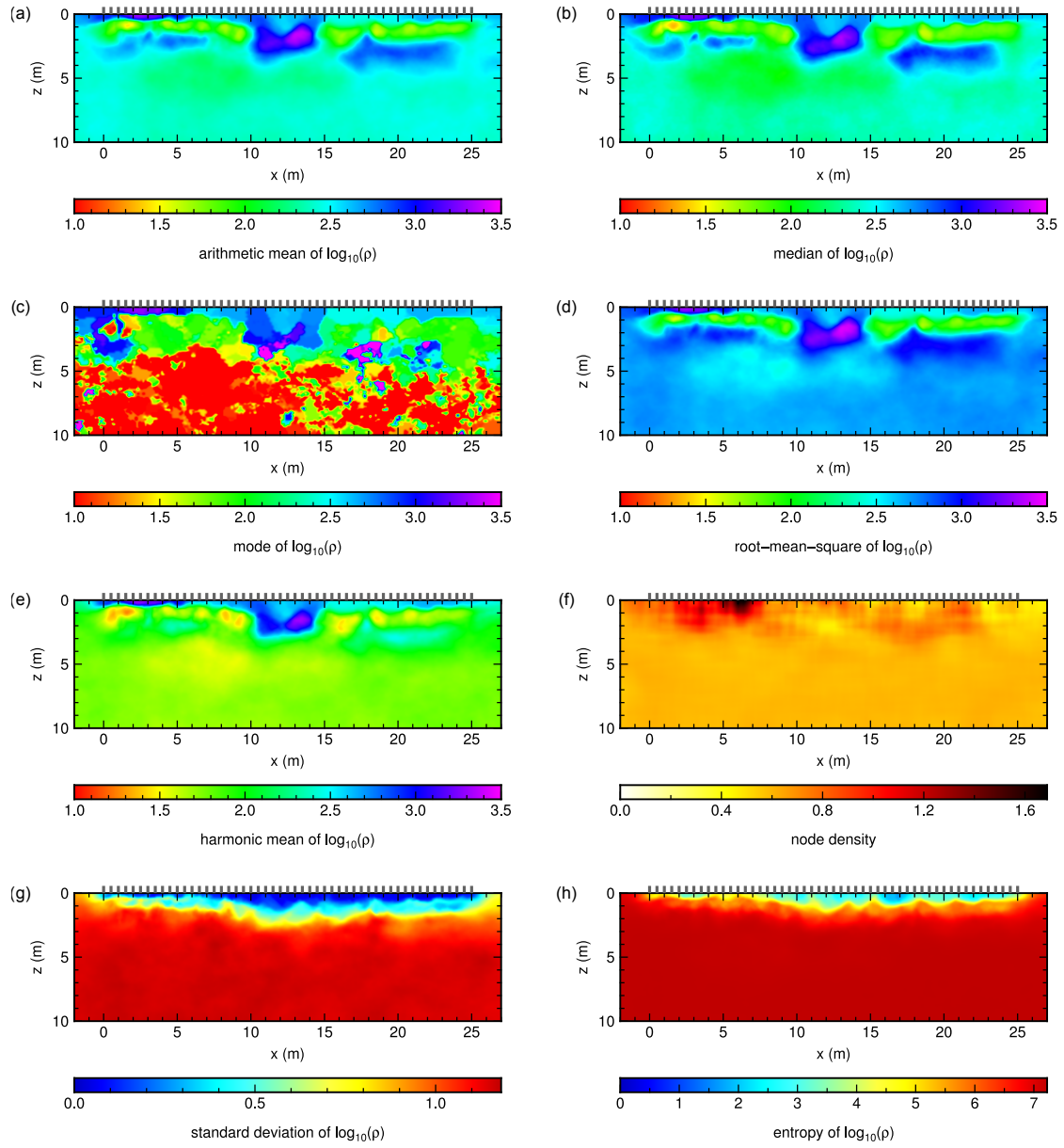

Figure S2. Inversion results for the Slovakia observational dataset found using the TERT algorithm. (a) Arithmetic mean. (b) Median. (c) Mode (i.e., maximum-a-posteriori). (d) Root-mean-square. (e) Harmonic mean. (f) Node density (measured within a 2 m $\times$ 2 m square sector centred on each pixel). (g) Standard deviation. (h) Entropy. Note that the colour scale in (a)–(e) is clipped between 1 and 3.5 to aid visualisation. In all panels, the grey ticks at $z = 0$ m denote electrode locations.

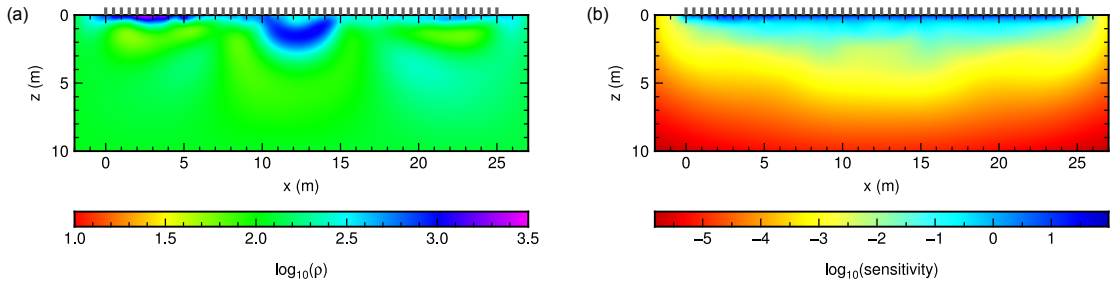

Figure S3. Inversion results for the Slovakia observational dataset found using the iterated-linearised code *R2* by *Binley* [2013]. (a) Best-fit resistivity map. (b) Sensitivity map. In both panels, the grey ticks at $z = 0$ m denote electrode locations.

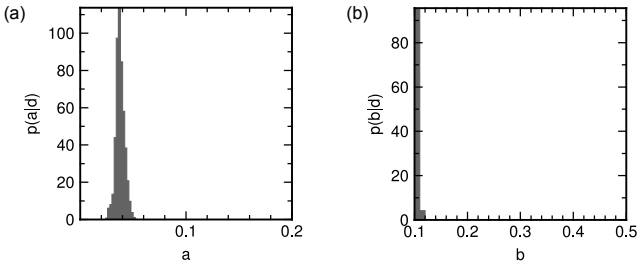

Figure S4. Posterior PDF on noise hyperparameters (a) a and (b) b for the Slovakia observational dataset obtained from TERT.